Application of Molecular Dynamics (MD) in Material Science and Engineering

Presented by -

- Nikhil Gupta 190005026
- Ishan Bharti 190005019
- Ankit Pandey 190005004
- Piyush Nimbhore 190005028
- Pradumn Patidar 190005030
- Ayush Nath 190005009

Introduction

- Molecular dynamics (MD) is a computer simulation method for analyzing the physical movements of atoms and molecules. The atoms and molecules are allowed to interact for a fixed period of time, giving a view of the dynamic "evolution" of the system.

- The trajectories of atoms and molecules are determined by numerically solving Newton's equations of motion for a system of interacting particles, where forces between the particles and their potential energies are often calculated using interatomic potentials or molecular mechanics force fields.

- Molecular Dynamics follows deterministic modelling which yields the exact same results for a particular sets of inputs, no matter how many times one recalculates the model.

Introduction

- The essence of molecular dynamics resides in the connection between the macroscopic world and the microscopic world provided by the theory of statistical mechanics.
- Quantitative and qualitative information about the macroscopic behaviour of macromolecules can be obtained from the simulation of a system at the atomistic level.
- MD has also been termed "statistical mechanics by numbers" and "Laplace's vision of Newtonian Mechanics" of predicting the future by animating nature's forces and allowing insight into molecular motion on an atomic scale.

History of MD

- MD was originally developed in the early 1950s, following the earlier successes with Monte Carlo Simulations but was popularized for statistical mechanics at Los Alamos National Laboratory by Rosenbluth and Metropolis.
- In an attempt to understand the origin of irreversibility, Fermi proposed in 1953, the use of MANIAC I, to solve the time evolution of the equations of motion for a many-body system subject to several choices of force laws.
- In 1956, Alder and Wainwright used an IBM 704 computer to simulate perfectly elastic collisions between hard spheres.

History of MD

- In 1960, in perhaps the first realistic simulation of matter, Gibson simulated radiation damage of solid copper by using a Born–Mayer type of repulsive interaction along with a cohesive surface force.
- In 1964, Rahman published simulations of liquid argon that used a Lennard-Jones potential; calculations of system properties, such as the coefficient of self-diffusion, compared well with experimental data.
- In 1967, L. Verlet published simulations on properties of Ar using LJ potential and also introduced the Verlet integration algorithm.

Flow Chart for Molecular Dynamics program

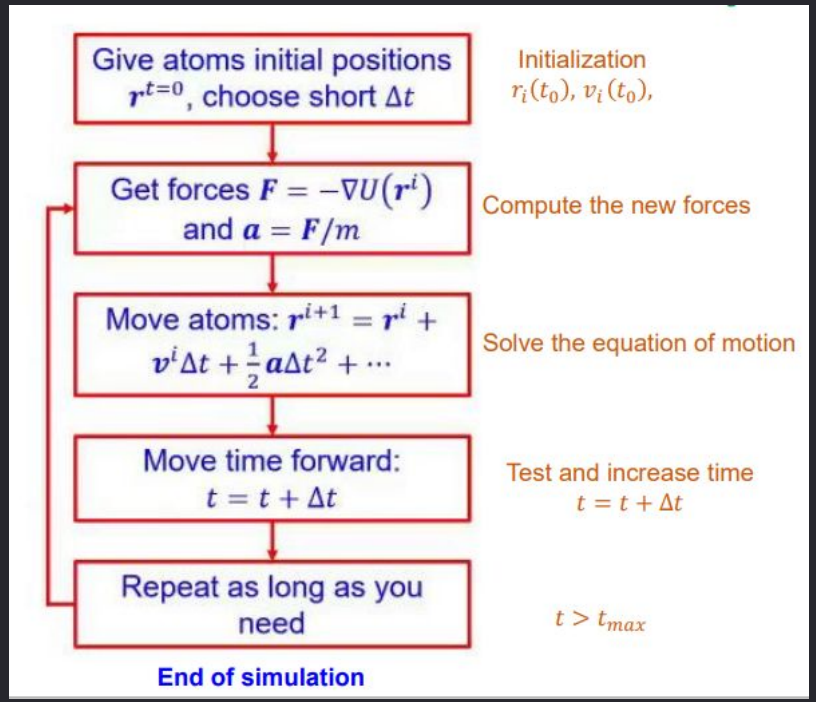

Predicts how particles move with time under certain conditions

- Create an Initial state
- Introduce Interaction potential
- Predict how particle move

Molecular Dynamics Procedure

1. Choose initial positions for the atoms
2. Choose an initial set of atom velocities. These are usually chosen to obey a Boltzmann distribution for some temperature, then normalized so that the momentum for the entire system is zero.
3. Compute the momentum of each atom from its velocity and mass
4. Compute the forces on each atom from the energy expression. This is usually a molecular dynamics force field designed to be used in dynamical simulations.

Molecular Dynamics Procedure

5. Compute new positions for the atoms a short time step (Δ t). This is a numerical integration of Newton's equations of motion using the information obtained in the previous steps.

6. Compute new velocity and accelerations for the atoms.

7. Repeat steps 3. through 6.

8. Repeat this iteration long enough for the system to reach equilibrium. In this case, equilibrium is not the lowest energy configuration; it is configuration that is reasonable for the system with the given amount of energy.

Molecular Dynamics Procedure

9. Once the system has reached equilibrium, begin saving the atomic coordinates every iterations. This list of coordinates over time is called a trajectory.

10. Continue iterating and saving data until enough data have been collected to give results with the desired accuracy.

11. Analyze the trajectories to obtain information about the system. This might be determined by computing radial distribution functions, diffusion coefficients, vibrational motions, or any other property computable from this information.

Verlet algorithm derivation

Initial {r(t), v(t)} → Final {r(t+Δt), v(t+Δt)}

- Derived from two Taylor expansions

$$r(t+\delta t) = r(t) + \frac{dr(t)}{dt}\delta t + \frac{1}{2}\frac{d^2r(t)}{dt^2}\delta t^2 + \frac{1}{3!}\frac{d^3r(t)}{dt^3}\delta t^3 + O(\delta t^4)$$

$$r(t-\delta t) = r(t) - \frac{dr(t)}{dt}\delta t + \frac{1}{2}\frac{d^2r(t)}{dt^2}\delta t^2 - \frac{1}{3!}\frac{d^3r(t)}{dt^3}\delta t^3 + O(\delta t^4)$$

- Add together and simplify

$$r(t+\delta t) = 2r(t) - r(t-\delta t) + \frac{d^2r(t)}{dt^2}\delta t^2 + O(\delta t^4)$$

Verlet algorithm derivation

- Velocities not explicitly solved, calculated typically from first order central difference.

$$v(t) = \frac{r(t+\delta t) - r(t-\delta t)}{2\delta t}$$

- Position vector at t+δt requires position
- Previous two time steps; a two-step method; not self starting

Advantages :

- Simplicity and good stability
- Global error $O(\delta t^2)$

Velocity Verlet Algorithm

Here there is

- Improved accuracy compared to standard Verlet
- Start with position and velocity expansions

$$r(t+\delta t) = r(t) + v(t)\delta t + \frac{1}{2}a(t)\delta t^2 \ldots$$

$$v(t+\delta t) = v(t) + \frac{1}{2}\delta t[a(t) + a(t+\delta t] + \ \ldots$$

Each integration cycle -

1. Calculate velocities at mid-step
2. Calculate positions at the next step
3. Calculate accelerations at next step from the potential
4. Update the velocities

$$v\left(t+\frac{\delta t}{2}\right) = v(t) + \frac{1}{2}a(t)\delta t$$

$$r(t+\delta t) = r(t) + v(t+\frac{\delta t}{2})\delta t$$

$$v(t+\delta t) = v\left(t+\frac{\delta t}{2}\right) + \frac{1}{2}a(t+\delta t)\delta t$$

The Leap-Frog Algorithm

- The velocities are first calculated at the time t+1/2 δt and using this velocities, position r obtained at time t+δt.
- The advantage of this algorithm is that the velocities are explicitly calculated
- The disadvantage is that they are not calculated at the same time as the positions

$$r(t_0 + \delta t) = r(t_0) + v\left(t_0 + \frac{1}{2}\delta t\right)\delta t$$

$$v\left(t_0 + \frac{1}{2}\delta t\right) = v\left(t_0 - \frac{1}{2}\delta t\right) + a(t_0)\delta t$$

- The velocities at time t can be approximated by:

$$v(t_0) = \frac{1}{2}\left[v\left(t_0 - \frac{1}{2}\delta t\right) + \left(t_0 + \frac{1}{2}\delta t\right)\right]$$

Gear's Predictor-corrector Algorithms

- Predict $a^c(t+\delta t)$ from the Taylor expansion at the starting point. Begin with a simple prediction, as in any of the previous methods. Initially step to $r(t+\delta t)$, $v(t+\delta t)$, $a(t+\delta t)$, $b(t+\delta t)$ at that point. The difference between the $a(t+\delta t)$ and the predicted $a^c(t+\delta t)$:

$$\Delta a(t+\delta t) = a^c(t+\delta t) - a(t+\delta t)$$

- Now use the error calculated in the previous step to correct all next step values

$$r^c(t+\delta t)=r^p(t+\delta t) + c_0\Delta a(t+\delta t)$$
$$v^c(t+\delta t)=v^p(t+\delta t) + c_1\Delta a(t+\delta t)$$
$$a^c(t+\delta t)=a^p(t+\delta t) + c_2\Delta a(t+\delta t)$$
$$b^c(t+\delta t)=b^p(t+\delta t) + c_3\Delta a(t+\delta t)$$

Beeman's Algorithm

Beeman's algorithm uses positions, velocities, and accelerations from the previous time step. This algorithm is closely related to the Verlet algorithm. According to that the respective position and velocity can be described by,

$$r(t_0 + \delta t) = r(t_0) + v(t_0)\delta t + \frac{2}{3}a(t_0)\delta t^2 - \frac{1}{6}a(t_0 - \delta t)\delta t^2$$

$$v(t_0 + \delta t) = v(t_0) + v(t_0)\delta t + \frac{1}{3}a(t_0)\delta t + \frac{5}{6}a(t_0)\delta t - \frac{1}{6}a(t_0 - \delta t)\delta t^2$$

The advantage of this algorithm is that it provides a more accurate expression for the velocities and better energy conservation. The disadvantage is that the more complex expressions make the calculations more expensive

Introduction to LAMMPS Software

LAMMPS (Large-scale Atomic/Molecular Massively Parallel Simulator) -

- Is a Classical Molecular Dynamics Program with a focus on Materials Modeling developed Under Sandia National Laboratories.
- It is a Model system with only a few particles up to millions or billions (depends on computational power) and capable for Atomic, polyatomic, biological, metallic, granular system.
- LAMMPS makes use of Message Passing (MPI) for parallel communication and is free and open-source software, distributed under the terms of the GNU General Public License Interface.
- Unlike Other Software For MD, LAMMPS Is Very "Modular" And Can Do Many Things In Many Different Ways And Is Used For Simulating Fluids, Metals And Other Materials In Molecular Level.

Overview of LAMMPS Simulation

Input - Data

- Initial positions
- Initial velocities
- Units
- Boundary Conditions (PBC)
- Potential energy function
- Ensemble

Running

- Molecular dynamics simulation
- Minimization

Output

- Trajectories
- Velocities
- Forces
- Energy of the system
- Temperature
- Pressure
- Density

Application Fields of LAMMPS

- Solid Mechanics
- Material Sciences
- Granular Flows
- BioPhysics
- Quantum Chemistry

18

Why LAMMPS ??

1. VERSATILITY -

- bio, materials, mesoscale
- Atomistic, coarse-grained, continuum

2. GREAT PARALLEL PERFORMANCE

3. EASIER TO EXTEND

4. WELL DOCUMENTED -

- Extensive Website
- 1200 Page Manual

5. ACTIVE AND SUPPORTIVE USER COMMUNITY -

- 40K postings to mail list, 1000+ subscribers
- Quick turn-around on Questions posted to mail list

MD Simulation Example-1

- ## Abstract

  This example shows how to run an atomistic simulation of uniaxial tensile loading of an aluminium single crystal oriented in the <100> direction.

- ## Description of Simulation

  This LAMMPS molecular dynamics simulation first generates a simulation cell with fcc atoms with <100> orientations in the x, y, and z-directions. The equilibration step allows the lattice to expand to a temperature of 300 K with a pressure of 0 bar at each simulation cell boundary. Then, the simulation cell is deformed in the x-direction at a strain rate of 10s-1 , while the lateral boundaries are controlled using the NPT equations of motion to zero pressure. The stress and strain values are output to a separate file, which can be imported in a graphing application for plotting.

Simulation Code

```
# Input file for uniaxial tensile loading of single crystal aluminum
# -------------------- INITIALIZATION ----------------------------
units           metal
dimension       3
boundary        p       p       p
atom_style      atomic
variable latparam equal 4.05

# ----------------------- ATOM DEFINITION ----------------------------
lattice         fcc ${latparam}
region          whole block 0 10 0 10 0 10
create_box      1 whole
lattice         fcc ${latparam} orient x 1 0 0 orient y 0 1 0 orient z 0 0 1
create_atoms    1 region whole

# ------------------------ FORCE FIELDS ------------------------------
pair_style      eam/alloy
pair_coeff      * * Al99.eam.alloy Al

# ------------------------- SETTINGS ---------------------------------
compute csym all centro/atom fcc
compute peratom all pe/atom

#######################################
# EQUILIBRATION
reset_timestep  0
timestep 0.001
velocity all create 300 12345 mom yes rot no
fix 1 all npt temp 300 300 1 iso 0 0 1 drag 1

# Set thermo output
thermo 1000
thermo_style custom step lx ly lz press pxx pyy pzz pe temp

# Run for at least 10 picosecond (assuming 1 fs timestep)
run 20000
unfix 1

# Store final cell length for strain calculations
variable tmp equal "lx"
variable L0 equal ${tmp}
print "Initial Length, L0: ${L0}"
```

Simulation Code

```
#####################################
# DEFORMATION
reset_timestep  0

fix             1 all npt temp 300 300 1 y 0 0 1 z 0 0 1 drag 1
variable srate equal 1.0e10
variable srate1 equal "v_srate / 1.0e12"
fix             2 all deform 1 x erate ${srate1} units box remap x

# Output strain and stress info to file
# for units metal, pressure is in [bars] = 100 [kPa] = 1/10000 [GPa]
# p2, p3, p4 are in GPa
variable strain equal "(lx - v_L0)/v_L0"
variable p1 equal "v_strain"
variable p2 equal "-pxx/10000"
variable p3 equal "-pyy/10000"
variable p4 equal "-pzz/10000"
fix def1 all print 100 "${p1} ${p2} ${p3} ${p4}" file Al_SC_100.def1.txt screen no

# Use cfg for AtomEye
dump            1 all cfg 250 dump.tensile_*.cfg mass type xs ys zs c_csym c_peratom fx fy fz
dump_modify 1 element Al

# Display thermo
thermo  1000
thermo_style    custom step v_strain temp v_p2 v_p3 v_p4 ke pe press

run             20000

#####################################
# SIMULATION DONE
print "All done"
```

MD Simulation Example-1

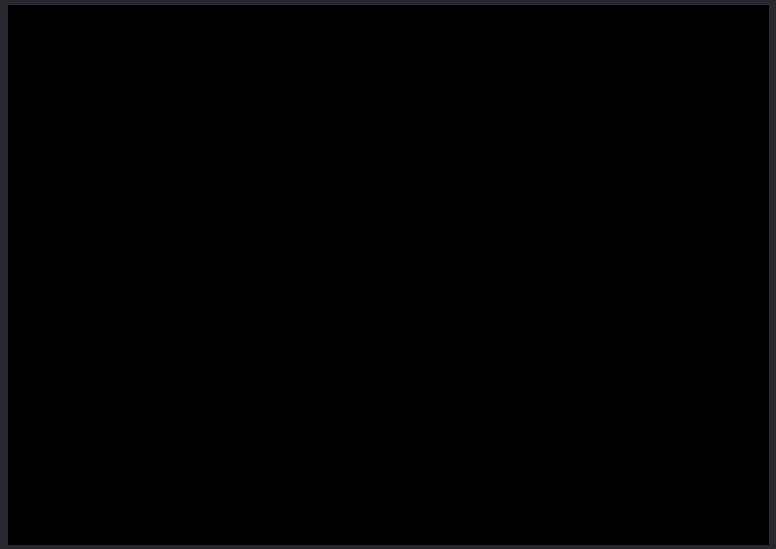

Using OVITO Visualization Tool, the molecular deformation can be observed

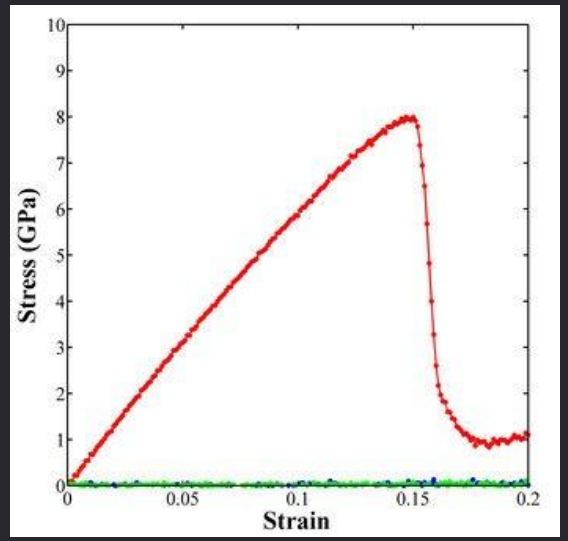

Fig.1- “File Al_SC_100.def1.txt “ is created after simulation. Using the MATLAB software the stress-strain curve is plotted.

MD Simulation Example-2

- Abstract:

  The objective of this tutorial is to generate a symmetric tilt grain boundary in LAMMPS. This tutorial can serve as a precursor to more advanced techniques, whereby in-plane translations and atom deletion criteria are used to sample a large number of potential structures to find the global minimum energy grain boundary structure.

- Description of Simulation:

  This LAMMPS molecular dynamics simulation first generates a simulation cell with fcc atoms with two blocks of differing orientations to create the grain boundary. The potential used is the Mishin et al. (1999) aluminum potential. The cfg dump files include the x, y, and z coordinates, the centrosymmetry values, the potential energies, and forces for each atom. This can be directly visualized using OVITO.

Simulation Code

```
# LAMMPS Input File for Grain Boundaries
# This file will generate a single Sigma5(310) STGB

# ---------- Initialize Simulation ---------------------
clear
units metal
dimension 3
boundary p p p
atom_style atomic

# ---------- Create Atomistic Structure ---------------------
lattice fcc 4.05
region whole block 0.000000 12.807225 -64.0361225 64.0361225 0.000000 4.050000 units box
create_box 2 whole
region upper block INF INF 0.000000 64.0361225 INF INF units box
lattice fcc 4.05 orient x  0  3  1 orient y  0 -1  3 orient z  1  0  0
create_atoms 1 region upper
region lower block INF INF -64.0361225 0.000000 INF INF units box
lattice fcc 4.05 orient x  0  3 -1 orient y  0  1  3 orient z  1  0  0
create_atoms 2 region lower
group upper type 1
group lower type 2

# ---------- Define Interatomic Potential ---------------------
pair_style eam/alloy
pair_coeff * * Al99.eam.alloy Al Al
neighbor 2.0 bin
neigh_modify delay 10 check yes

# ---------- Displace atoms and delete overlapping atoms ---------------------
displace_atoms upper move 0 0 0 units lattice
delete_atoms overlap 0.35 lower upper

# ---------- Define Settings ---------------------
compute csym all centro/atom fcc
compute eng all pe/atom
compute eatoms all reduce sum c_eng
```

Simulation Code

```
# ---------- Run Minimization ---------------------
reset_timestep 0
thermo 10
thermo_style custom step pe lx ly lz press pxx pyy pzz c_eatoms
dump            1 all cfg 25 dump.sig5_minimization_*.cfg mass type xs ys zs c_csym c_eng fx fy fz
dump_modify     1 element Al Al
min_style cg
minimize 1e-15 1e-15 5000 5000
undump 1

# ---------- Run Minimization 2---------------------
# Now allow the box to expand/contract perpendicular to the grain boundary
reset_timestep 0
thermo 10
thermo_style custom step pe lx ly lz press pxx pyy pzz c_eatoms
fix 1 all box/relax y 0 vmax 0.001
min_style cg
minimize 1e-15 1e-15 5000 5000

# ---------- Calculate GB Energy ---------------------
variable minimumenergy equal -3.360000
variable esum equal "v_minimumenergy * count(all)"
variable xseng equal "c_eatoms - (v_minimumenergy * count(all))"
variable gbarea equal "lx * lz * 2"
variable gbe equal "(c_eatoms - (v_minimumenergy * count(all)))/v_gbarea"
variable gbemJm2 equal ${gbe}*16021.7733
variable gbernd equal round(${gbemJm2})
print "GB energy is ${gbemJm2} mJ/m^2"

# ---------- Dump data into Data file -------------
reset_timestep 0
dump            1 all cfg 10000 dump.al_sig5_310_*.cfg mass type xs ys zs c_csym c_eng fx fy fz
dump_modify     1 element Al Al
minimize 1e-15 1e-15 5000 5000
undump 1

write_restart restart.al_sig5_310_stgb

print "All done"
```

Output

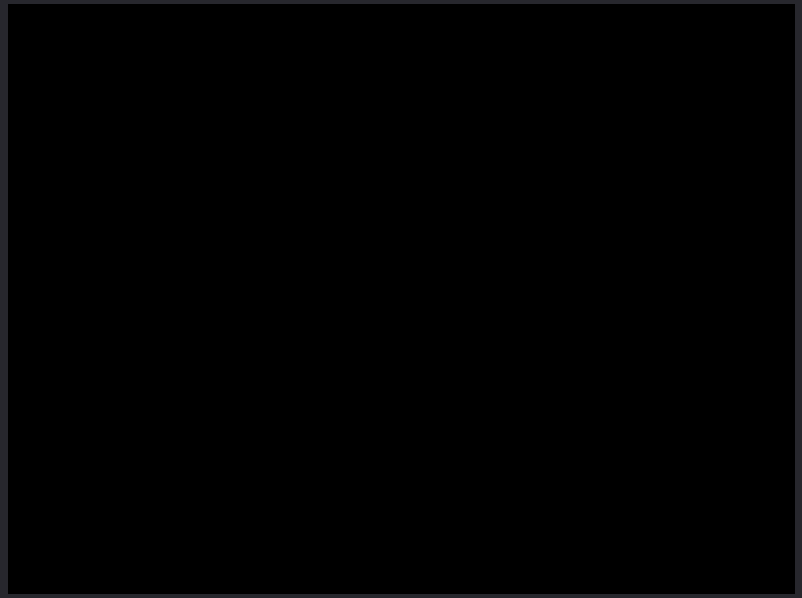

Using OVITO Visualization Tool, the molecular deformation has been observed

After calculation, GB Energy was found to be the value 564.16610218266 mJ/m^2 in the log file.

Research Paper Presentations

Molecular Dynamics

Molecular dynamics studies of CNT-reinforced aluminum composites under uniaxial tensile loading

Name : Nikhil Gupta
Roll No. : 190005026

Abstract

This paper investigates the mechanical behavior of carbon nanotube (CNT)-reinforced aluminum composites (CNT-Al composites) under a tensile loading condition using molecular dynamics (MD) simulations.

It highlights the benefits of CNT-Al composites from a structural point of view. This study shows that, compared to pure aluminum, the Young's moduli are improved by 31% for (4,4)CNT-Al, 33% for (6,6)CNT-Al, and 39% for (8,8)CNT-Al. Moreover, the corresponding toughness values are significantly enhanced by 37%, 72%, and 100%.

Furthermore, the MD simulations provide insights into various fracture behaviors at the atomic scale, including lattice disordering, local changes in lattice structures due to stacking faults, and void nucleation/growth. The component analysis shows that the mechanical properties of CNT-Al composites improve significantly, even with a small amount of CNT, due to the considerable load-bearing capacity of CNT.

Introduction

After the discovery of carbon nanotubes (CNTs), the materials have been extensively studied and utilized in various scientific and engineering applications due to their novel structural and electronic properties. These properties enable remarkable potential applications of CNTs as nano-electronics, quantum wire interconnects, field emission devices, composites, chemical sensors, bio-sensors, and detectors. As a reinforcing agent, CNTs have superior characteristics of low density (1.3 g/cm^3), a high Young's modulus (~1 TPa), high tensile strength (50-150 GPa), and failure strain (~20%).

Atomic simulations, such as molecular dynamics (MD) simulations, have been widely used to predict the mechanical properties of nano-scale structures. Particularly for the study of failure mechanisms, MD simulations have significant advantages due to the capability of capturing dynamic atomic behaviors.

Introduction

Using MD simulation, on investigating the effect of a Ni coating on CNT surfaces with regard to the mechanical strengthening of CNT-Al composites, the Young's modulus of the CNT-Al composite increased with the density of the Ni coatings, because the Ni coating provided an effective channel for load transfer between the CNT and Al matrix.

On studying the effects of vacancy defects of CNTs on the fracture behavior of CNT-Al composites, the study illustrated that even a one atom vacancy defect dramatically reduced the failure stresses and strains.

On studying the compressive behavior of CNT-Al composites using MD simulation, the increase in Young's modulus due to the inclusion of CNT ranged from 50% to 100%, compared to that of pure Al was reported.

Introduction

On conducting a series of MD simulations to investigate the mechanical behaviors of CNT-Al composites under uniaxial tensile loading, the simulations shed light on detailed fracture mechanisms, including plastic deformation and crack evolution inside the composite, at the atomic scale.

The component analysis reveals the considerable contribution of CNT as a load-bearing material, despite its small volume fraction. In addition, quantitative information on the mechanical properties is provided that shows the effect of CNT diameter.

Computational Methods

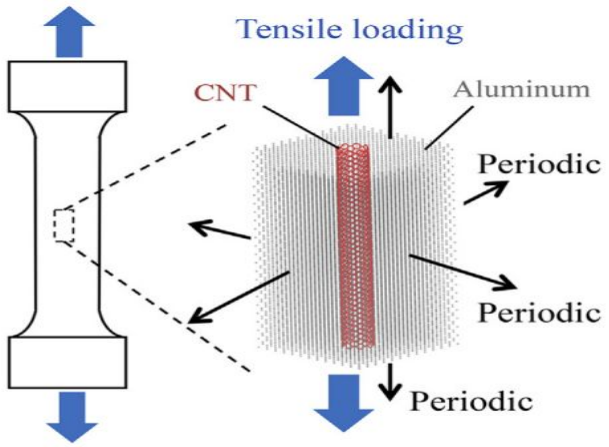

Fig. 1. Schematic of the atomic model for MD simulations, representing the inside of a CNT—Al composite specimen under tensile loading.

In the above figure, in order to represent the nano-scale structure inside a CNT-Al composite, periodic boundary conditions (PBCs) are applied in the x, y, and z directions. By adopting omnidirectional PBCs, a representative volume inside a composite under a tensile test can be accurately described.

Computational Methods

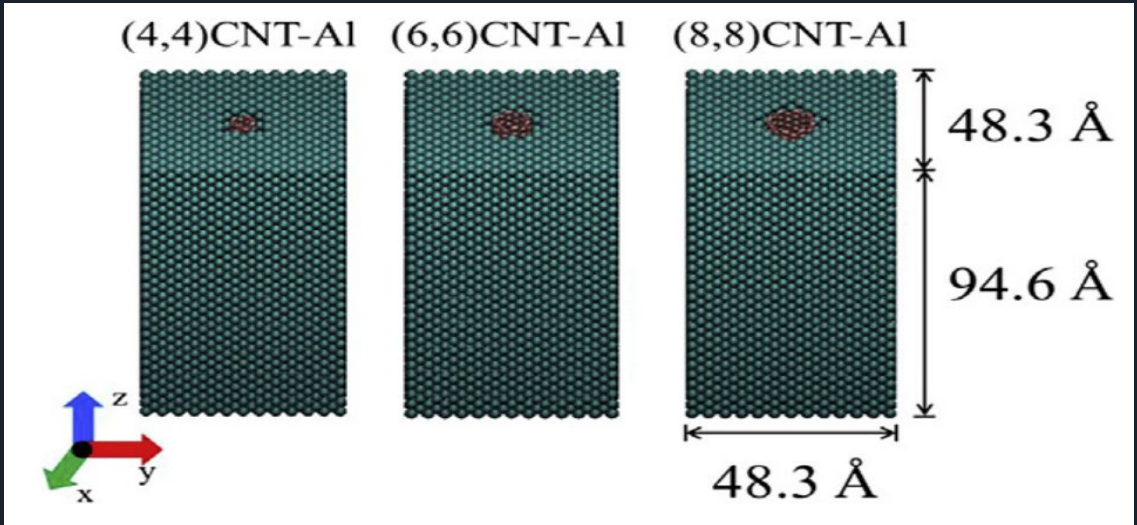

The simulations are performed for three different models as shown in above figure. All three models have the same Al matrix geometry with various CNT diameters. The cyan and red atoms denote aluminum and carbon, respectively. The Al matrices are in a square prism shape with the dimensions of 48.3 Å*48.3 Å*94.6 Å. The armchair nanotubes of (4,4)CNT-Al, (6,6)CNT-Al, and (8,8)CNT-Al are placed inside holes of 5.4 Å, 8.1 Å, and 10.8 Å diameter, respectively.

Results and Discussion

The snapshots of the MD simulations are presented to show the overall characteristics of the fracture process during the tensile simulation are as follows :

(A) The below figure (a) shows an equilibrated state before tensile strain is applied to the system (Strain =0).
(B) The below figure (b) shows that at a strain of around 0.1, the CNT moves from the center (Strain=0.11).
(C) In figure (c), as the strain increases, a void grows near the top of the aluminum matrix and is accompanied by atomic disorder (Strain= 0.15).

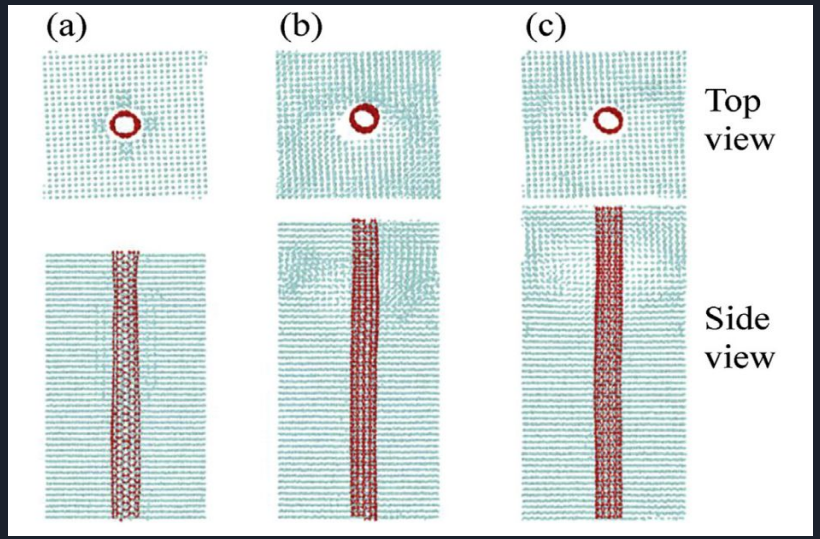

Results and Discussion

(D) Next, at a strain of approximately 0.2, the CNT breaks near the void , which continues to enlarge and ultimately results in the system separating into two parts.

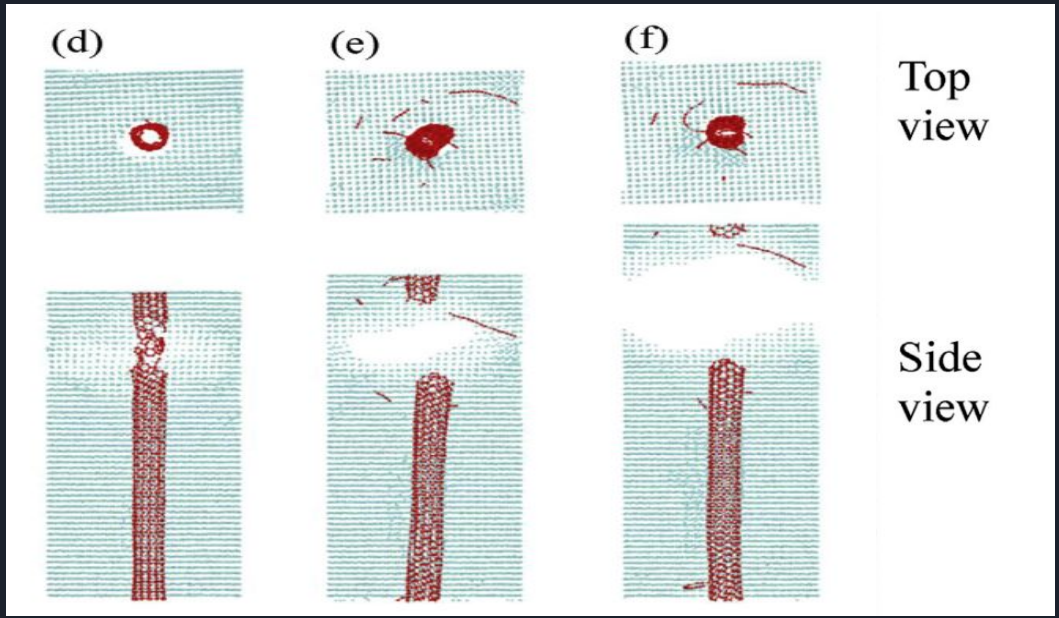

Snapshots of the MD simulations during the loading process at various strains of (d) 0.19, (e) 0.25, and (f) 0.45.

Results and Discussion

In the adjacent figure, the calculated stress-strain curve is shown. The red, green, blue, and black curves represent the stress-strain curves of (4,4)CNT-Al, (6,6)CNT-Al, (8,8)CNT-Al, and pure aluminium, respectively.

In the region of strain in range of 0 -0.07, the relation between stress and strain is almost linear for all materials.

The calculated Young's moduli of (4,4)CNT-Al, (6,6)CNT-Al, and (8,8) CNT-Al are 97.01 GPa, 99.02 GPa, and 103.3 GPa, respectively, showing that the Young's moduli increases as the CNT diameter increases. The Young's modulus of pure aluminum is calculated to be 74.24 GPa.

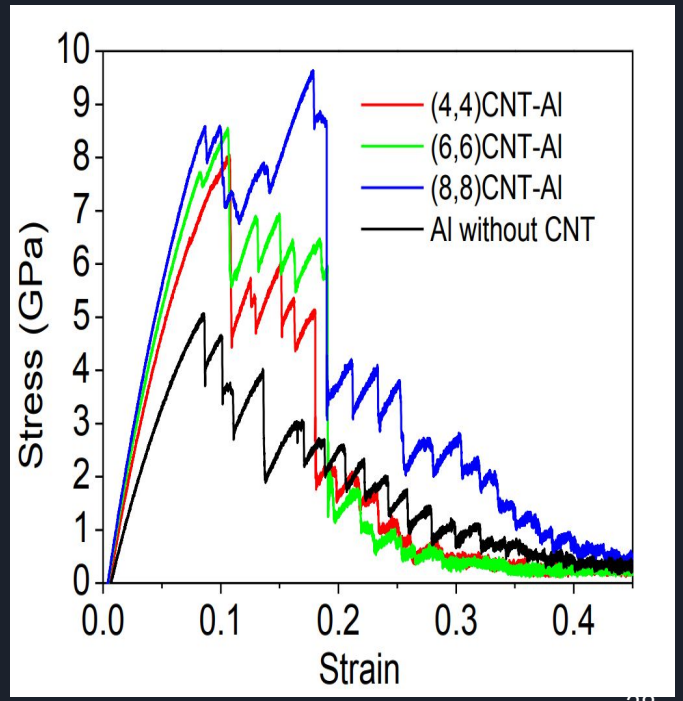

Results and Discussion

Therefore, compared to pure Al, the elasticity of the CNT-Al composites of (4,4)CNT-Al, (6,6)CNT-Al, and (8,8) CNT-Al improves by 31%, 33%, and 39%, respectively due to CNT. The level of improvement is eventually significant, considering that the amount of CNT is less than 5% of the total volume fraction.

The most dramatic change with increase in CNT diameter is composite toughness. Particularly, the area under the curve between the 0.1 and 0.2 strain values largely increases according to CNT size. Compared to the toughness of pure aluminum, toughness increases of 37% for (4,4)CNT-Al, 72% for (6,6)CNT-Al, and 100% for (8,8)CNT-Al were observed. The 2%, 3%, and 4% volume fraction of CNT contributes to the total energy absorption of approximately 30%, 40%, and 50%, respectively. The calculations reveal that only a small percentage of CNT reinforcement contributes to a dramatic increase in load support.

Results and Discussion

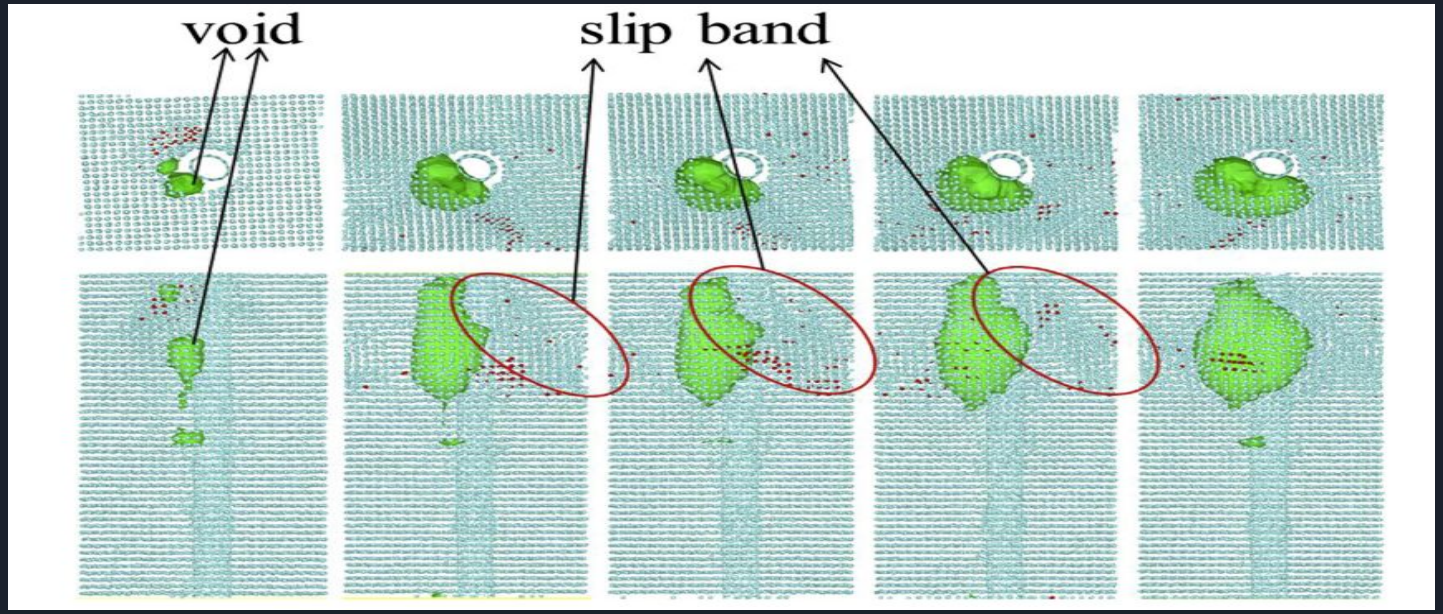

In the above figure, snapshots of the MD simulation around 0.1 strain is shown, where the stress-strain curve shows a large decrease. The snapshots show the detailed mechanisms of fracture evolution inside the aluminum matrix. The green denotes a void, and the red represents the HCP lattice structure.

Results and Discussion

Around a strain of 0.2, the CNT fracture process are captured in the adjacent figure. First, the two C-C bonds parallel to the applied loading begin to break near the void in the aluminum matrix. Next, the bond breakage spreads, and the hole expands on the surface. The fracture then propagates perpendicular to the loading direction, eventually leading to a complete break of the CNT.

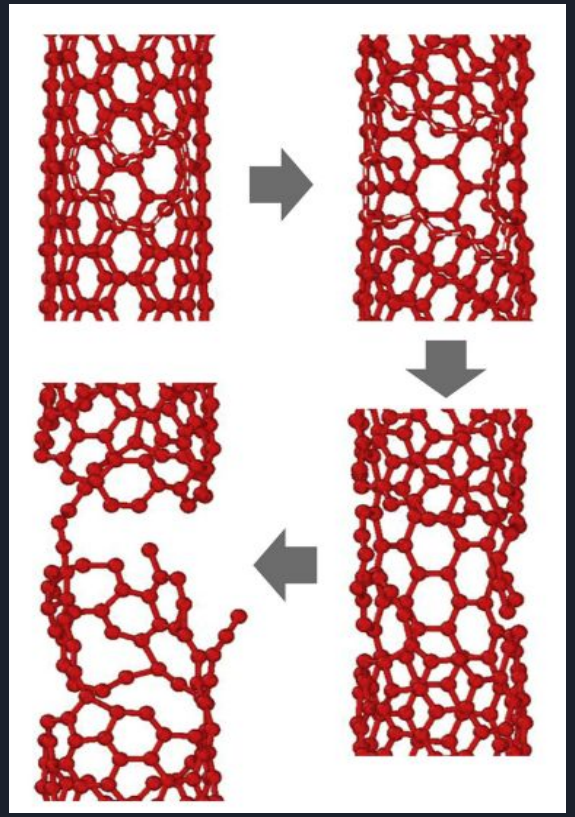

Conclusions

In the present study, MD simulations were conducted in order to investigate the mechanical behavior of CNT-reinforced aluminum composite with various CNT diameters. The stress-strain curves were obtained under tensile loading, and the variations of the curves were analyzed through MD snapshots that enable detailed analyses of atomic behaviors.

The overall mechanical properties, such as Young's modulus and toughness, increased considerably as the CNT reinforcement was increased. Furthermore, component analysis revealed that even a small fraction of CNT can play a significant role in enhancing the mechanical properties of composites. Although excessive external loading can fracture the metal matrix and initiate a crack inside the metal matrix, CNTs withstand additional loading and thereby suspend the entire fracture of the composite by increasing the fracture strain almost two-fold.

Conclusions

In addition, the MD simulations offered a detailed fracture mechanism of the MMCs at the atomic scale. For example, the stress decreases were shown to be due to the combination of lattice structure change, dislocation, stacking faults, and micro-void nucleation, whereas these phenomena are rarely observed in real-world experiments.

This study provides a theoretical framework for predicting the mechanical behaviors of MMCs at the atomic scale. The model in this study can be used to investigate the effects of CNT defects, CNT surface coatings, CNT orientations, and different types of CNTs and matrices on the mechanical properties of MMCs.

It is of considerable significance that these studies at the atomic scale will reveal the fundamental factors that define the macroscale properties. A multiscale model will be developed to characterize the mechanical properties of MMCs by combining the MD model and a continuum model. It will be a model that can be used to design bulk MMCs with desirable mechanical properties by tailoring the nanoscale variables.

References

Molecular dynamics studies of CNT-reinforced aluminum composites under uniaxial tensile loading

- By Bong Kyu Choi , Gil Ho Yoon, Seungjun Lee

https://www.sciencedirect.com/science/article/pii/S1359836816000263

Thank You

Molecular dynamics simulations of tensile deformation of gradient nano-grained copper film

Presented by - Ishan Bharti
190005019

Overview

Molecular dynamics simulations are performed to investigate the plastic deformation of a gradient nano Grained (GNG) copper film. An extra strengthening is observed in the GNG film which indicates there is synergetic interaction between different grain-size layers. The plastic deformation of the GNG film occurs first in small grains and then propagates into larger grains with increasing strain. This orderly plastic deformation process is attributed to the GNG structure and found independent of strain rate and temperature. Grain coarsening induced by the deformation is apparently suppressed in the GNG film due to the GNG structure

Introduction

Nano-grained (NG) metals usually exhibit several times higher in strength than their coarse-grained counterparts but a very low tensile ductility. Gradient microstructures, in which the grain size increases along the depth from nanoscale to microscale, have been found to be an effective strategy to improve the ductility of nano-structured metals.

The plastic deformation of a copper sample with a gradient microstructure was observed to occur orderly from coarse grains to small grains with increasing loads.

Strength-ductility synergy was also achieved in some engineering alloys with the GNG structures.

In order to investigate the mechanical behavior of metals and alloys with the GNG structure on their surface, a dislocation-based theoretical models is proposed.

The proposed theoretical models well captured the experimental results. Molecular dynamics (MD) simulations were also used to investigate the tensile deformation mechanism of Fe with the GNG structure and the fracture behavior of precracked nanocrystalline Ni with grain size gradients.

MD simulations have been widely used to investigate the plastic deformation of nanocrystalline metals.In this work MD simulations is used to investigate the atomistic deformation mechanism of GNG copper film. The simulation results reveal a different plastic deformation behavior of the GNG film in comparison with the GNG layer adherent on a coarse grained copper substrate.For the GNG film, the plastic deformation is observed gradually propagating from small grain-size layer to large grain-size layer with increasing strain. An extra strengthening induced by the GNG structure is also observed. Additionally, the influence of strain rates and temperature on the plastic deformation behavior of the GNG copper film is investigated.

Simulation details

MD simulations were carried out using the LAMMPS code.

An embedded-atom method (EAM) was used to describe the interaction between copper atoms. Three fully 3-dimensional models, i.e., one GNG model and two homogeneous NG models, were constructed using the Voronoi tessellation technique with random grain orientation containing no textures.

In order to simulate the uniaxial tension of GNG or NG films ,a periodic boundary condition was applied along the y and z-directions and non-periodic boundary condition was imposed in the x-direction during the MD simulations.Conjugate gradient method were performed on three models first, and then they were relaxed at 300 K for at least 50 ps using the NPT ensemble.

Fig. 1. The relaxed atomic configurations of the three models, i.e., the GNG film with grain sizes increasing from about 2.5 nm to 10.5 nm (a) and the NG films with mean grain sizes of 5.5 nm (b) and 10.5 nm (c). Non-periodic boundary condition is imposed along the x direction and Uniaxial tensile deformation is performed along the y direction.

Here green color represents perfect fcc atoms, red color represents perfect hcp atoms, and others represent the non-12-coordination atoms.

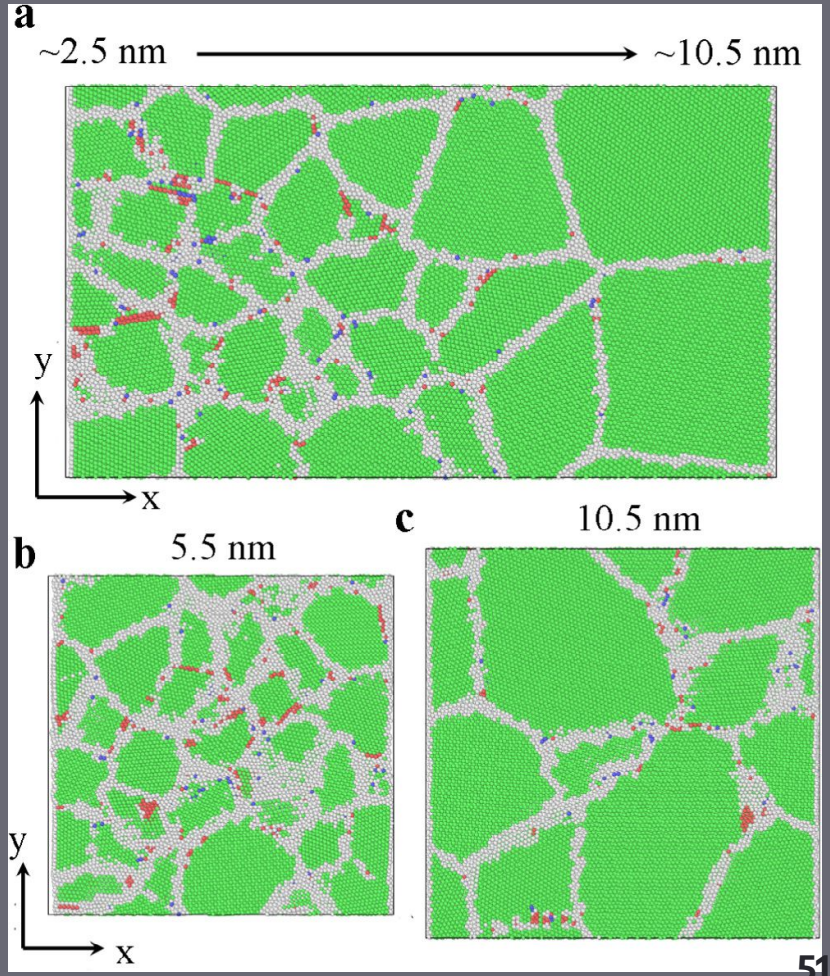

Results and discussion

Fig. 2 presents the simulated stress-strain curves of the GNG film and the homogeneous NG films with mean grain sizes of 5.5 nm and 10.5 nm. The strength of the GNG film is very close to that of the homogeneous 10.5-nm-film and obviously larger than that of the homogeneous 5.5-nm-film.According to the inverse Hall-Petch relation, the strength of NG metals should decrease with decreasing grain size when the grain size is smaller than about 10 nm.However, the simulation result shows the strength of the GNG film is nearly the same as that of the homogeneous 10.5-nm-film.

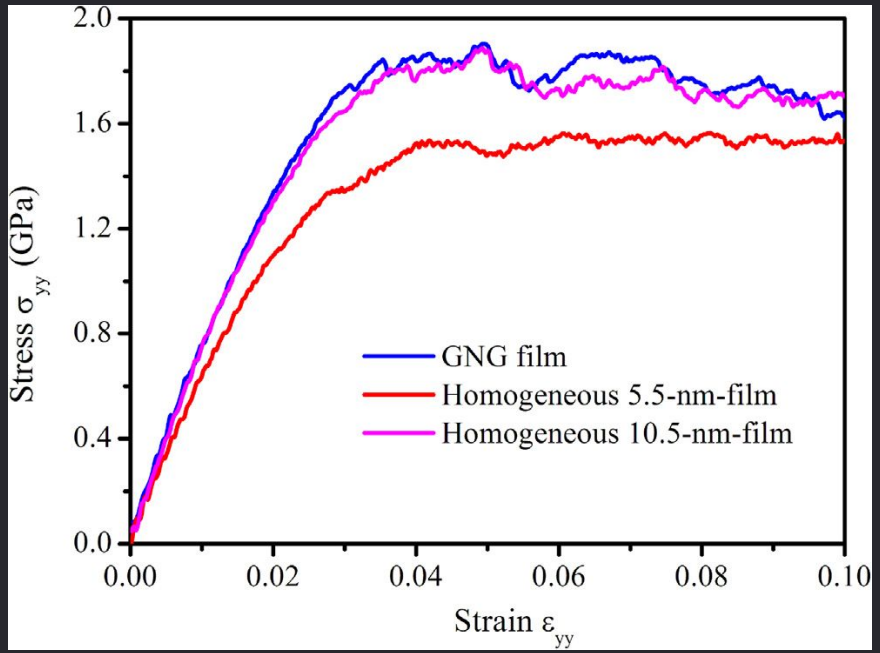

Fig. 2. The simulated stress-strain curves for the GNG film and the homogeneous NG films at a strain rate of 1 x 10^8 s^{-1} and 300 K.

Because of the GNG structure, the distribution of σ_{yy} should be inhomogeneous in the plane perpendicular to the tensile direction, i.e., the xz plane in the present simulation. In order to show this inhomogeneous distribution we divide the GNG film into three equal-thickness layers along the x direction (see the inset in Fig. 3) and calculate the mean atomic stress for the equal Thickness layers separately. The calculated results are shown in Fig. 3 for the strains of 3% and 6%, where we can see an inhomogeneous stress distribution.

The layer with larger grains has higher stress at both strains. And with increasing the strain from 3% to 6%, the stress of the middle layer increases fast to nearly the same value of the third layer. This observation also indicates the existence of a synergy of different layers with different grain sizes which induces the extra strength during the deformation.

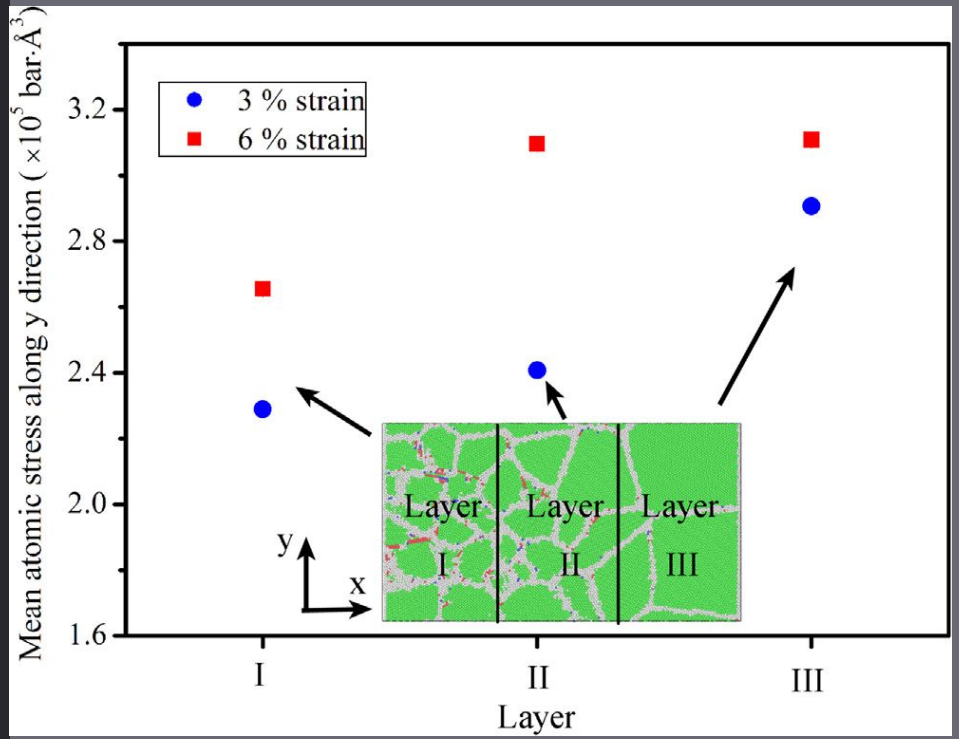

Fig. 3. Mean atomic stresses along y direction for three equal-thickness layers at strains of 3% and 6%. The inset illustrates the three equal-thickness layers along x direction.

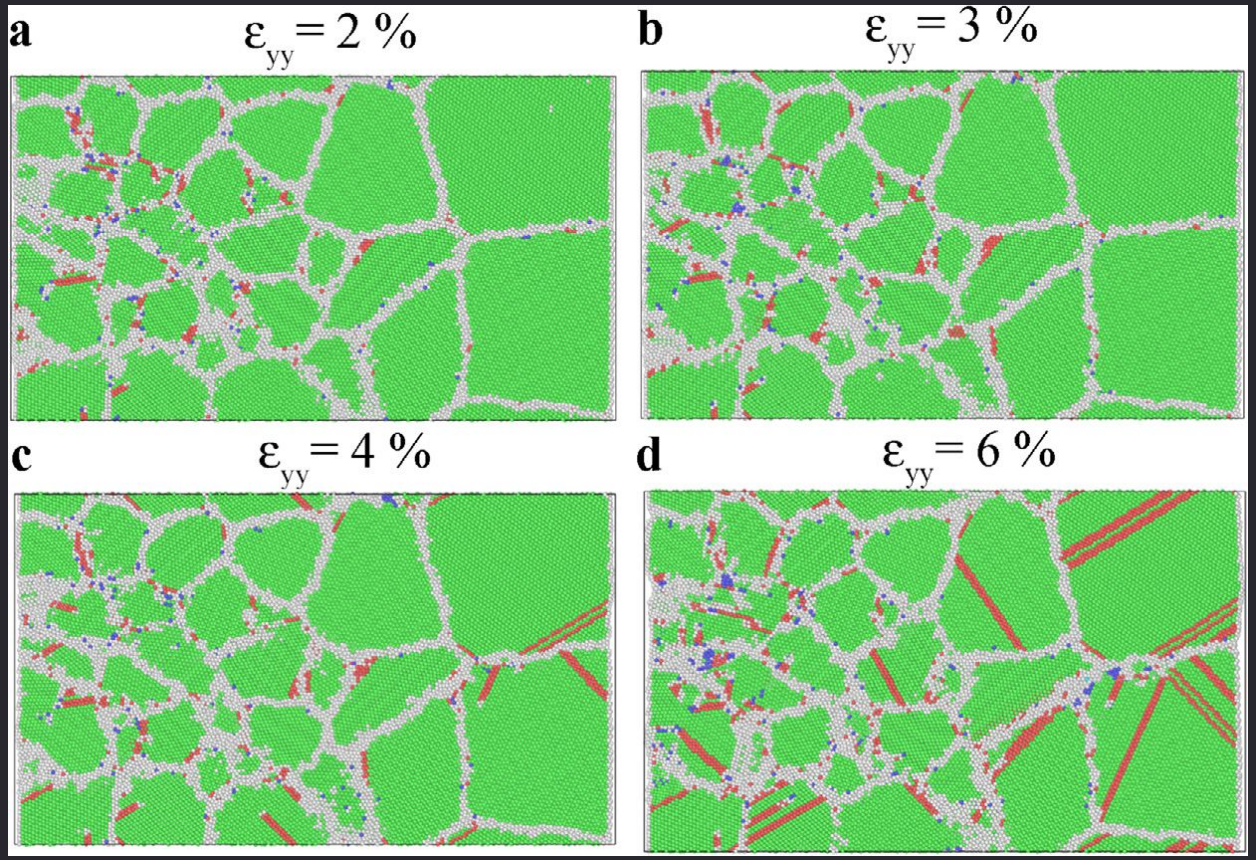

Fig. 4. Atomic configurations of the GNG film at tensile strains of (a) 2%, (b) 3%, (c) 4% and (d) 6%.

Fig.4. shows the dislocation nucleation and propagation in the GNG film during the tensile deformation. The dislocations always nucleate at grain boundaries and propagate into the grains leaving behind stacking faults.

It should be noted that the dislocation propagation already occurs in the small grains at 2% strain (see Fig. 4(a)), while no dislocation propagation can be seen in the largest grains even at 3% strain (see Fig. 4(b)). Until the strain is up to 4% the dislocation propagation can be observed in the largest grains (Fig. 4(c)). With further increasing the strain to 6% more dislocation activities can be observed in both small and large grains (Fig. 4(d)).

According to the observation shown in Fig. 4 we find that the plastic deformation of the GNG film does not occur simultaneously in different grains when under tension, but gradually from small grains to large grains with increasing loads. This is different to the homogeneous NG films where plastic deformation occurs almost simultaneously in grains with different sizes (Fig. 5)

Fig. 5. Atomic configurations of the NG films with mean grain sizes of ((a) and (b)) 5.5 nm and ((c) and (d)) 10.5 nm at strains of 3% and 6%.

This observation indicates that the GNG copper film is different from the GNG copper layer on a bulk Cu substrate where the grain growth was experimentally observed during the plastic deformation

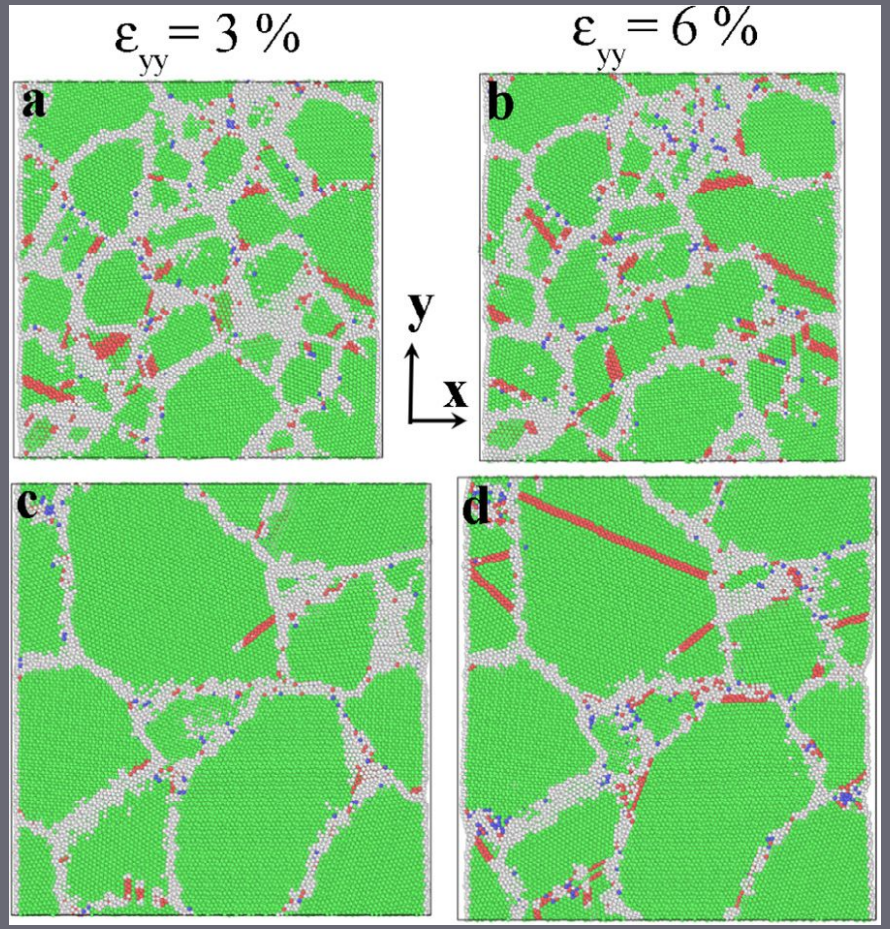

Fig. 6. presents the absolute values of the x and y components of atomic displacement of the GNG film at 3% strain relative to the initial positions.

Because the tensile direction is along the y direction, the GNG film will shrink along the x direction under uniaxial tension. From this Fig. 6 we can see that atoms belong to large grains have large atomic displacement along the x direction,which implies the strain along the x direction is inhomogeneous and a strain gradient can be formed along the x direction. In contrast, atomic displacement in the y direction occurs mainly near grain boundaries and distributes homogeneously throughout the GNG film.

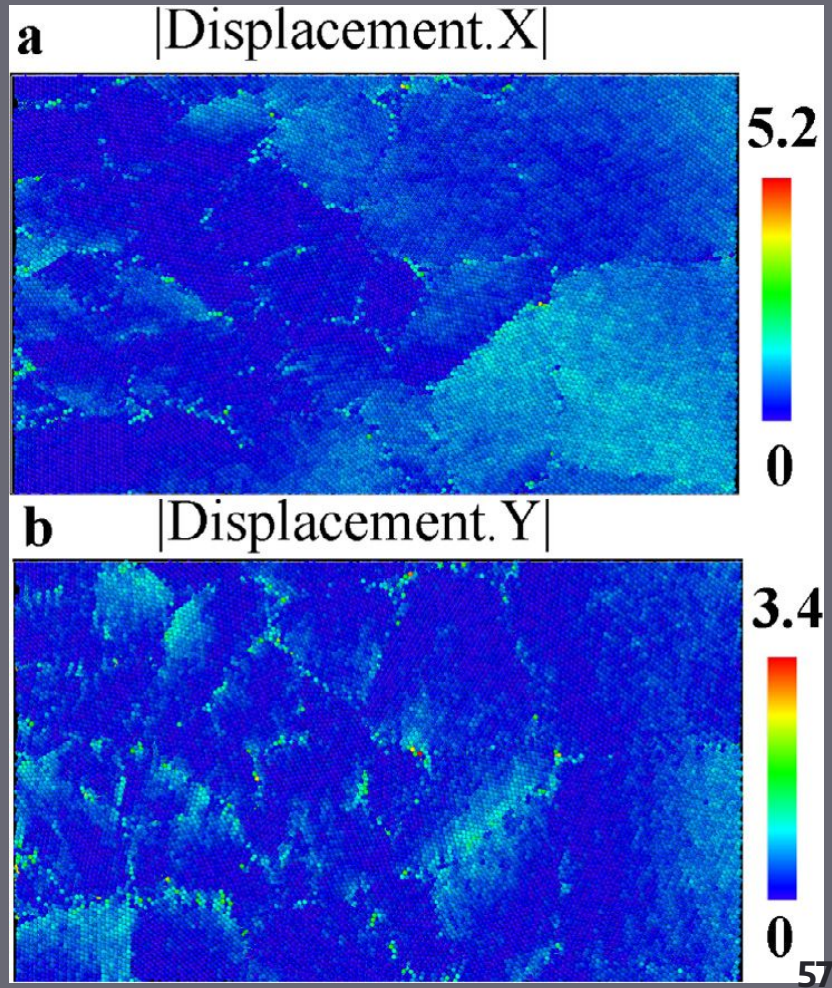

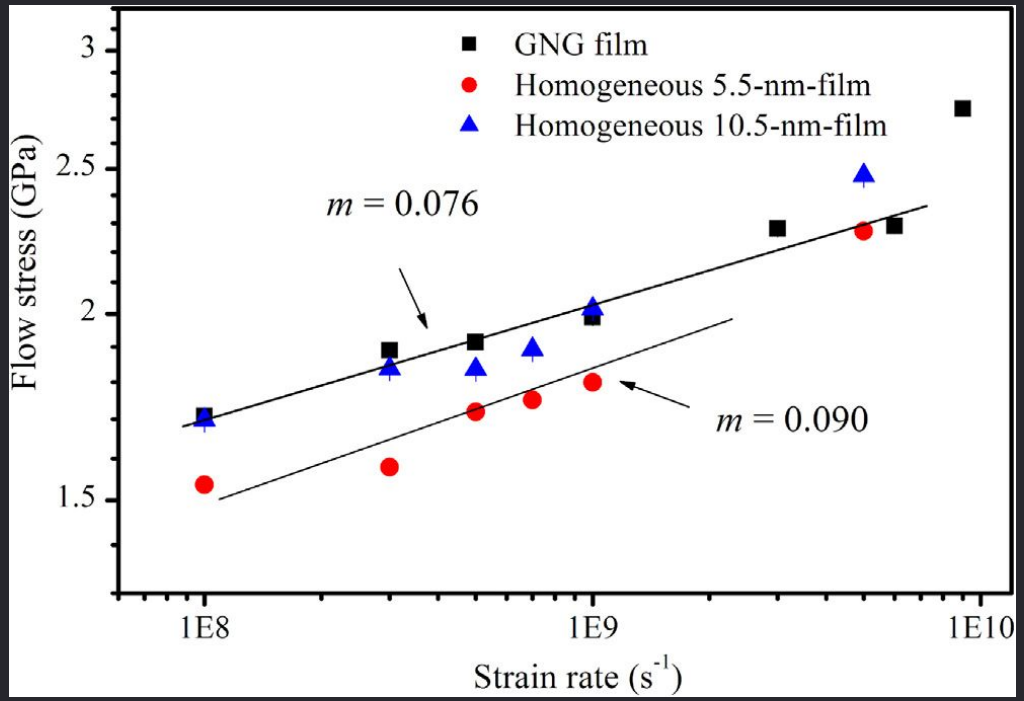

Strain rate effect on the plastic deformation of the GNG film is also investigated and the flow stress as a function of strain rates is presented in Fig. 7.

The strain rate sensitivity of the GNG film is close to that of the homogeneous 10.5-nm film but smaller than that of the homogeneous 5.5-nm film, as shown in Fig. 7.

Fig. 7. Double logarithmic plot of flow stress vs. strain rate for the GNG film ,the homogeneous NG films deformed at 300 K. The flow stress is the average stress in the strain range of 8–10%.

From Fig. 8. we can see that the plastic deformation also initially occurs in small grains and propagates into larger grains with increasing strain at a strain rate of $1 \times 10^9 s^{-1}$.

This indicates that the strain rate has no influence on the orderly plastic deformation induced by the gradient structure.

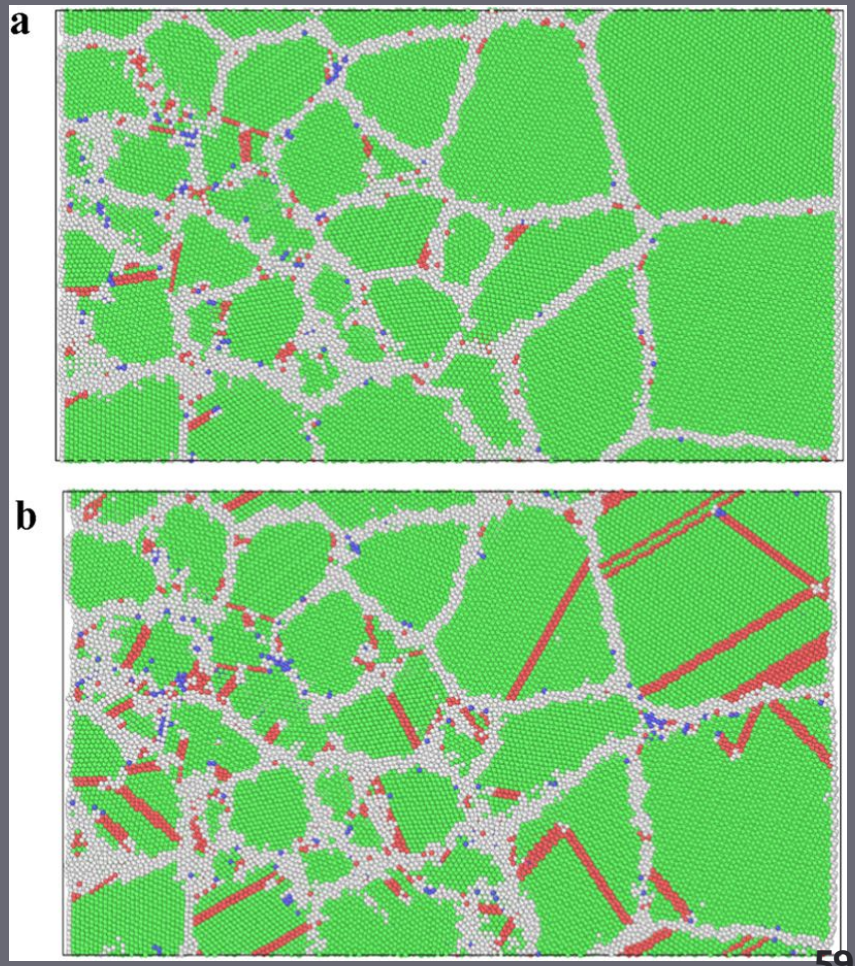

Fig. 8. Atomic configurations of the GNG film at (a) 3% and (b) 6% strain, deformed at a strain rate of $1 \times 10^9 s^{-1}$.

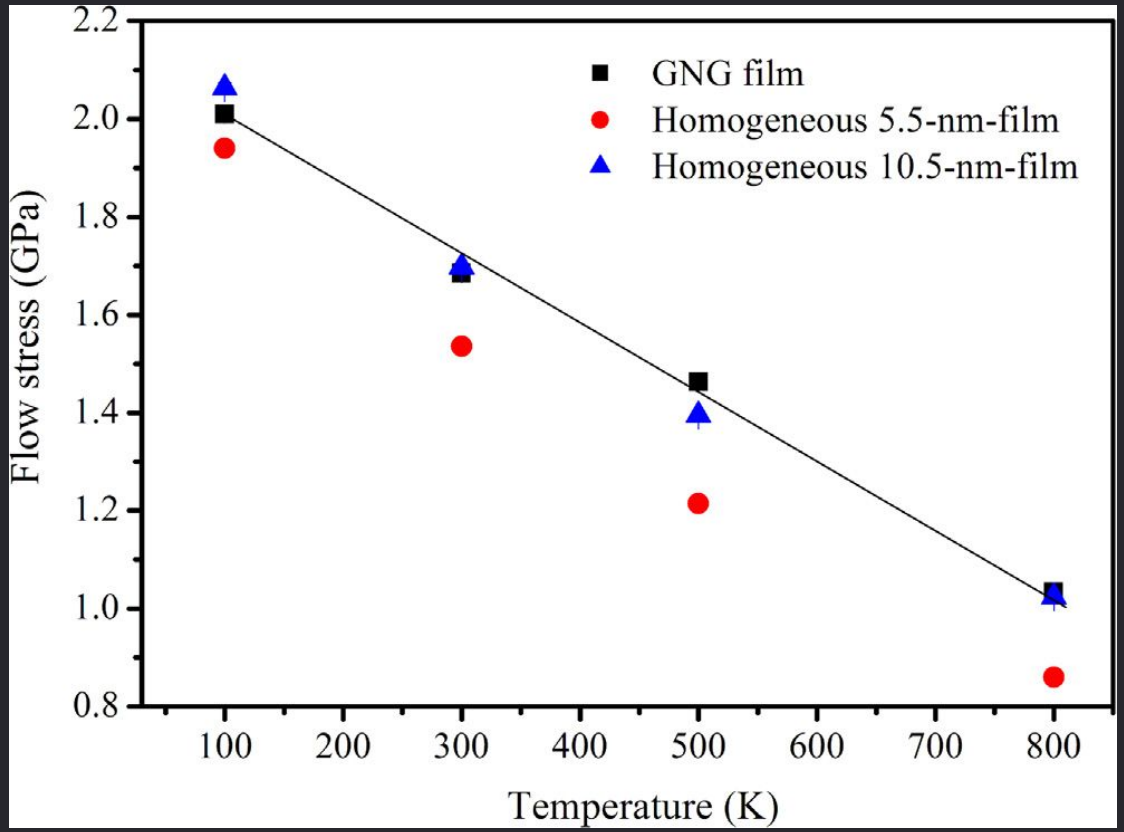

The flow stress of the GNG film and the homogeneous NG film as a function of temperature is presented in Fig. 9, where the flow stress decreases linearly with increasing temperature, indicating a softening of the GNG film and the homogeneous NG films with increasing temperature

Fig. 9. Flow stress vs. temperature for the GNG film and the homogeneous NG films deformed at 1 x 10^8 s^{-1}. The flow stress is the average stress in the strain range of 8–10%.

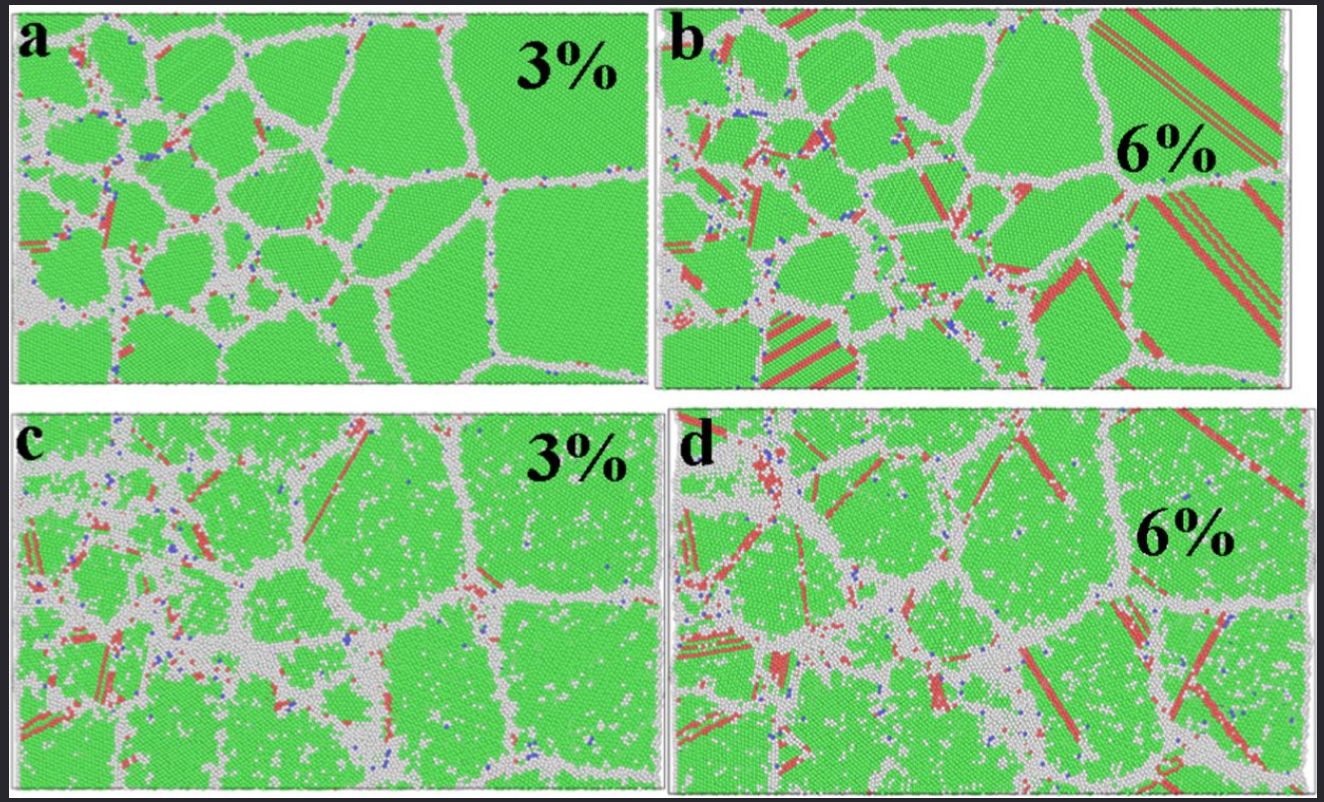

Fig. 10. Atomic configurations of the GNG film deformed at ((a) and (b)) 100 K and ((c) and (d)) 800 K. The corresponding strain is shown in the figure.

In order to show the plastic deformation process at different temperatures, atomic configurations of the GNG film at 3% and 6% strain deformed at 100 K and 800 K are presented in Fig. 10.

At both temperatures the plastic deformation occurs first at small grains and then propagates into larger grains with increasing strain. Temperature does not influence the orderly plastic deformation process at least in the present temperature range.

Conclusions

Uniaxial tensile deformation of the GNG film has been investigated by MD simulations. An extra strengthening induced by the GNG structure is observed in the GNG film.

Deformation induced grain coarsening is effectively suppressed by the GNG structure. The stress distribution in the cross section perpendicular to the tensile direction is inhomogeneous.

The onset of plastic deformation of the GNG film occurs first at small grains and then propagates into larger grains with increasing strain.This orderly plastic deformation is not influenced by strain rate and temperature.

The strain rate sensitivity of the GNG film is approximate to 0.076 calculated from the simulation results.

References

Molecular dynamics simulations of tensile deformation of gradient nano-grained copper film

By:- Kai Zhou *, Ting Zhang, Bin Liu, Yijun Yao

School of Physics and Optoelectronic Engineering,Nanjing University of Information Science & Technology, Nanjing 210044, China

https://www.sciencedirect.com/science/article/pii/S0927025617306079

Computational Materials Science

Volume 142, 1 February 2018, Pages 389-394

Thank You

Molecular dynamics study of the thermodynamic and kinetic properties of the solid-liquid interface in FeMn

By - **S.Ramana J.J.Hoytbd P.Saidic M.Astad**

190005004
Ankit Pandey

Abstract

The solid-liquid phase equilibria as a function of temperature and composition has been computed. Interaction between atoms were modeled using a second nearest neighbor modified embedded atom method potential.

In this Paper a new MD simulation method for computing solute trapping behavior that is able to access relatively low interface velocities. The segregation coefficient as a function of velocity for the Fe-Mn system was determined for three temperatures and the results are discussed within the framework of previously proposed theoretical models.

Introduction

- The combination of light weight,high strength and excellent ductility in Fe-Mn-Al-C steels is of particular interest in automotive design, where higher fuel efficiency and the decrease of greenhouse gas emissions are of paramount importance.
- Investigated the solidification cracking susceptibility in Fe-Mn-C and Fe-Mn-Al-C steels and found that cracking behavior depends on the segregation of Al and Mn in the dendritic microstructure.
- The phase field model has been shown to be a very effective tool for simulating the growth and solute segregation behavior of dendrites and dendrite arrays

- However, there are several material parameters required as input to the phase field model that are difficult to obtain from experiments.
- The measure the anisotropy of the interfacial free energy must be done, as it is critical for the accurate prediction of the dendrite velocity and morphology
- The solid-liquid interfacial free energy as a function of composition and temperature is computed for Fe-Mn alloys using molecular dynamics simulation.
- From free solidification MD simulations, the kinetic properties of the solid-liquid interface is described in terms of the solute trapping behavior as a function of interface velocity

Simulation Procedures

The interatomic potential reproduces fairly well various properties of Fe-Mn such as the lattice parameter and mixing enthalpies for the FCC solid and liquid phases. All MD simulations were performed using the LAMMPS code and a timestep of 1 fs was used throughout. In addition, a standard Nose-Hoover thermostat and barostat, with relaxation times of .1 ps and 1 ps respectively, were used for all simulations.

To determine the Fe-Mn phase diagram the approximate liquidus points were computed for a range of Mn compositions (5%, 10%,...30%). This first step involved the creation of solid-liquid systems where the composition was equal in both phases and estimating the temperature at which the phase fraction remains constant over the MD run.From the approximate temperatures, the next step in the phase diagram calculation utilized the semi-grand canonical (SGMC) feature of lammps. Here the chemical potential difference between Mn and Fe($\mu\Delta$) was fixed and atom type changes were attempted and accepted or rejected using the Metropolis algorithm.

Schematic of the MD simulation cell geometry before the solidification runs. The system is first equilibrated at some given temperature. There are then three ways to generate a solidification driving force:

- lowering of the system temperature,
- lowering the liquid portion in the center of the cell by a specified amount−ccΔeq,
- and varying the width of the regions adjacent to the interfaces (w1 and w2) where the concentration is not changed.

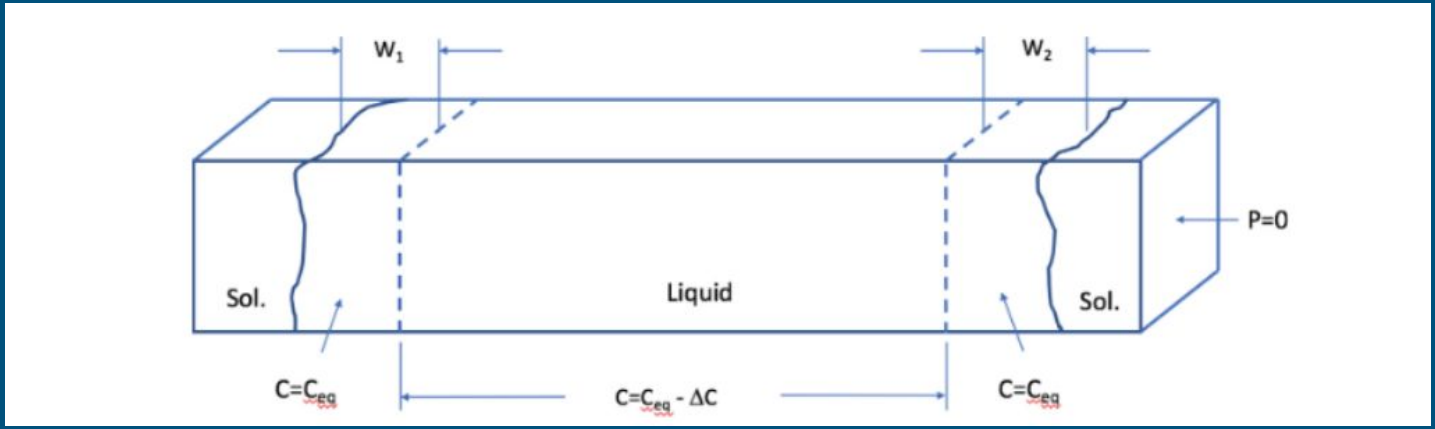

- A solid-liquid order parameter was assigned to each atom and then average over small bins along the long x dimension of the cell.

- The composition of the solid and liquid, and hence the segregation coefficient, is determined by constructing the coarse grained number density profiles for several MD snapshots over the time period when steady state motion is detected

- In both cases the temperature of the system was set to 1458 K

- The solid lines are guides to the eye and represent fits to an exponential decay of the concentration profile in the liquid.

- It is clear that the smaller window width corresponds to a higher velocity and a higher degree of solute trapping

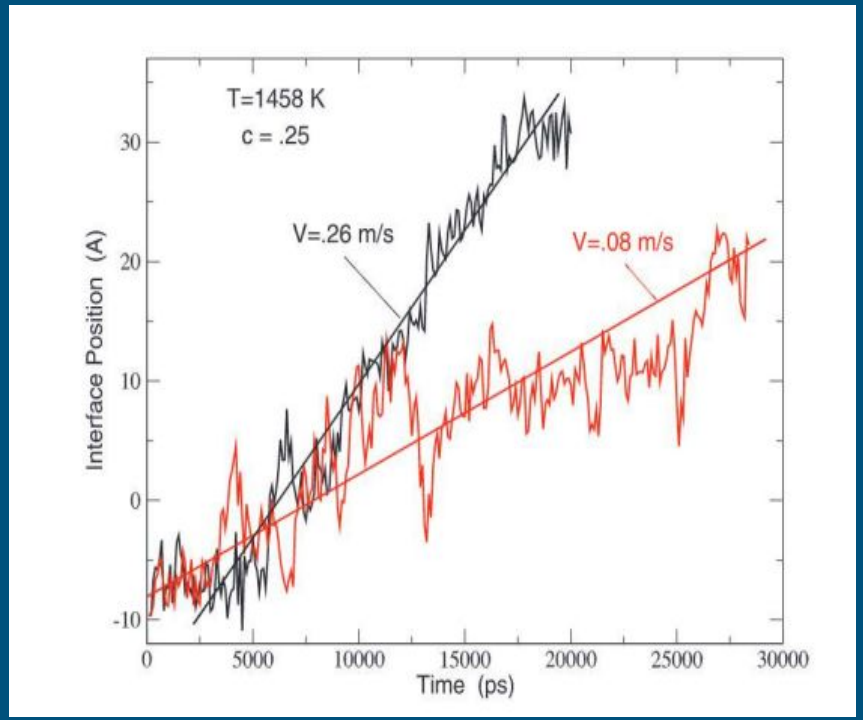

Interface position vs. time for two separate runs in the Fe-Mn system. In both cases the Mn concentration in the middle portion of the liquid was set to.25 (see Fig. 1)and the temperature was maintained at=T 1458K. However,the top curve corresponds to a window setting of w = 5 unit cells and the lower curve a width of w = 15 was used.

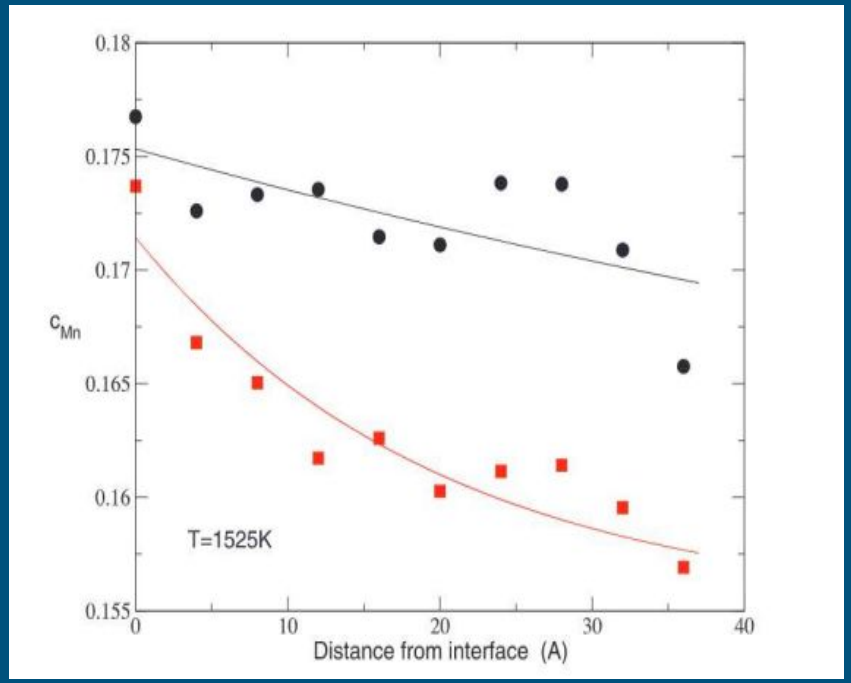

Steady state Mn concentration profiles in the liquid. The temperature for the runs was 1525 K and the initial concentration in the center of the liquid was0.155. The top curve refers to the case of a large window width and the bottom is the thin window.

Results and Discussions

- The solid-liquid portion of the phase diagram for the 2NN-MEAM Fe-Mn system is shown later. Both the solidus and liquidus lines shown in the plot represent quadratic polynomial fits to the data obtained from the SGMC procedure.

- The very small partitioning implies that the computation of the solute segregation vs. velocity behavior is very challenging

- Because the equilibrium BCC δ phase has not been computed here, but, as is clear from the extrapolation of the solidus and liquidus lines, the melting point of the pure FCC phase lies about 15 degrees below the experimental δ phase melting point and the solid-liquid coexistence lines for the atomistic model are shifted to lower temperatures.

- The excess interfacial free energy vs temperature for the Fe-Mn system as computed by the CFM. The most striking feature of the trend is the fact that, within statistical uncertainty,γ is essentially unchanged with temperature

- In the EAM systems Cu-Zr and Al-Sm, both glass forming binary alloys, the interfacial free energy increases substantially as the temperature is lowered.

- Therefore, it appears the Fe-Mn system represents an intermediate case where γ remains constant with temperature

- The interfacial energy for the final composition is in reasonable agreement with the MD results, the other two experimental data points are substantially higher

Temperature composition phase diagram of the 2NN-MEAM Fe-Mn potential showing the solid-liquid phase equilibria. The solidus and liquidus lines are polynomial fits to the data obtained from the SGMC simulations

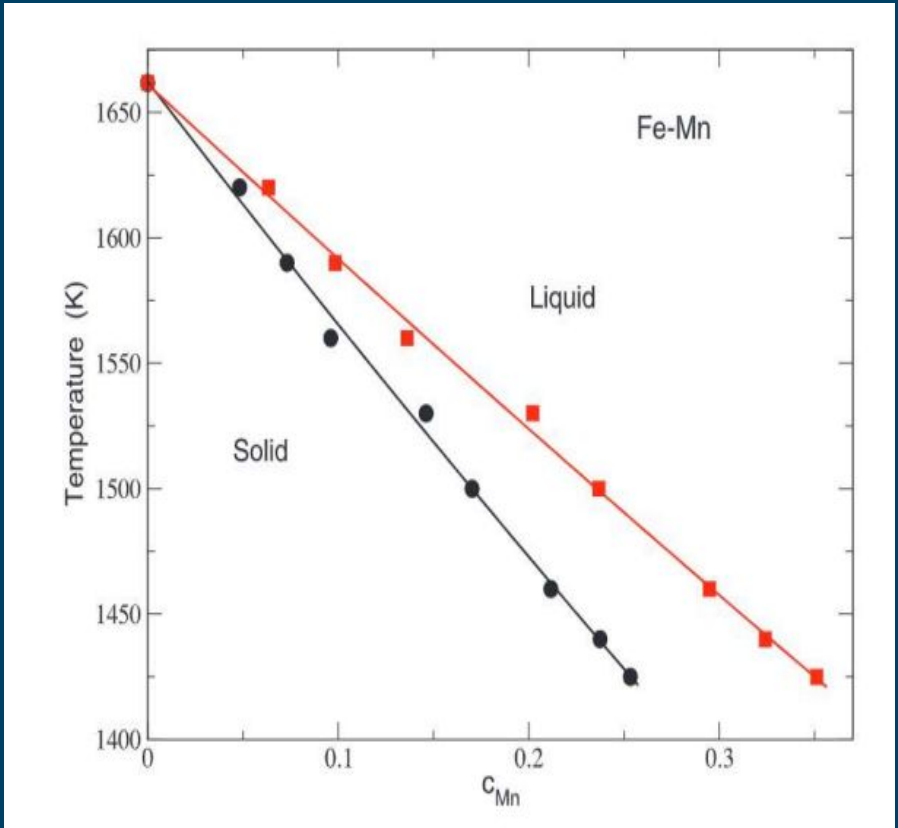

The solid-liquid interfacial free energy as a function of temperature for the Fe-Mn system

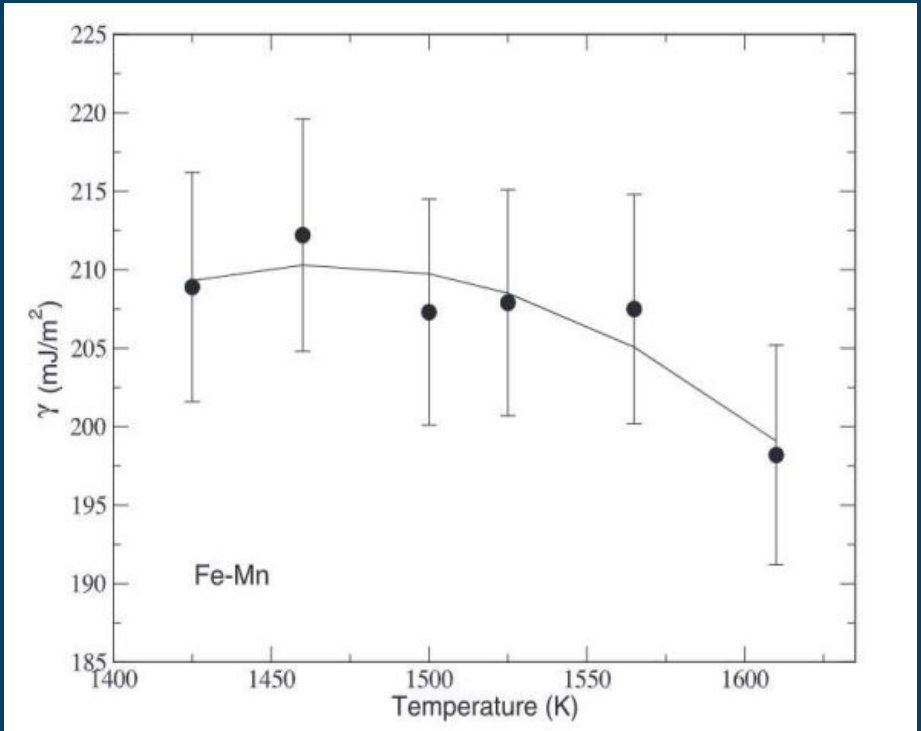

- The solvability theory of dendrite growth demonstrates that the dendrite tip radius and velocity depend strongly on the weak anisotropy of the solid-liquid interfacial free energy and thus the anisotropy is an important input parameter in phase field simulations

- The trend of the two anisotropy parameters as a function of temperature for the Fe-Mn system

- The top curve in the plot refers to ϵ_1 and the data is read from the left hand y axis. The ϵ_2 term is the bottom curve, which refers to the right ordinate.

- The behavior of the segregation coefficient vs the interface velocity is shown for the intermediate Mn concentration (T= 1525 K)system studied. As discussed above it is very difficult to compute kV() in Fe-Mn due to the very small equilibrium partitioning between the solid and liquid and this is manifest in the large scatter in the data.

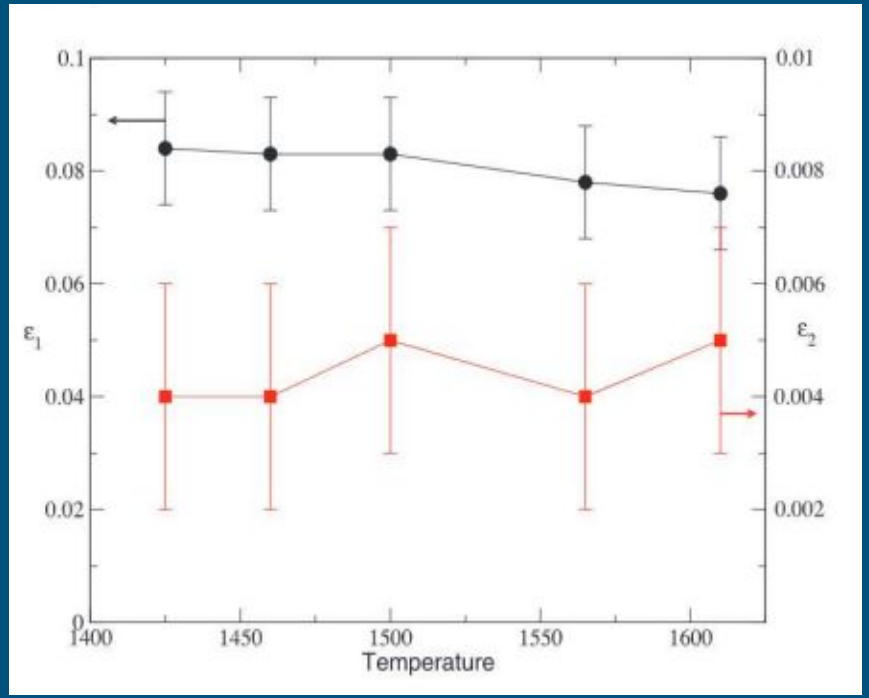

The two parameters describing the anisotropy of the solid-liquid interface in Fe-Mn. The top curve, which refers to the left ordinate, is the result for the ϵ_1 term. The bottom curve and right ordinate is the ϵ_2 parameter

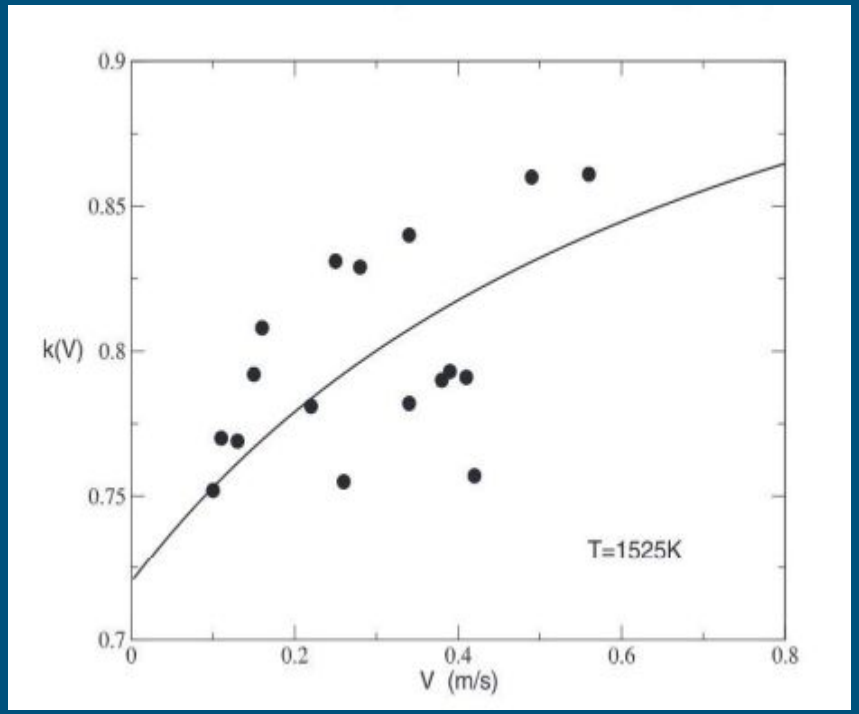

The segregation coefficient,k, vs the interface velocity at temperatures in the vicinity of=T1525K. The solid line is afit to the Aziz model, yielding a diffusive speed of V_d=0.75Dm/s.

Conclusion

- The second nearest neighbor MEAM potential for the Fe-Mn system exhibits an equilibrium phase diagram in qualitative agreement with experiment and reproduces quite well the small partitioning between the liquid and solid.

- In order to provide valuable input for modeling of solidification processes, the capillary fluctuation method was used to compute the solid-liquid interfacial free energy and its anisotropy as a function of composition and temperature.

- It was found that the averagevalueγ, as well as the anisotropy parameters ∈1 and ∈2 remain nearly constant with decreasing temperature.

- Finally, the solute trapping behavior at fairly low velocities was studied using a free solidification technique. The kV() function is characterized by the diffusive speed and we find VDvaries from≈ 1.1 m/s at T = 1603 K to.45 m/s at T = 1460 K. The variation of VD with temperature appears to be higher than the bulk liquid diffusion coefficient, highlighting the potential limitation of commonly used estimates for the trapping velocity.

Reference

Molecular dynamics study of the thermodynamic and kinetic properties of the solid-liquid interface in FeMn

Author S.Ramana J.J.Hoyt P.Saidic M.Asta

https://www.sciencedirect.com/science/article/pii/S0927025620302640

Thank You

Molecular Dynamics Simulations Of Substitutional Diffusion

BY –

X.W. Zhou , R.E. Jones, J. Gruber

Sandia National Laboratories, USA

Presented By -
190005028

PIYUSH NIMBHORE

ABSTRACT -

In Atomistic Simulations, Diffusion Energy Barriers Are Usually Calculated For Each Atomic Jump Path Using A Nudged Elastic Band Method.

It Is Often Preferred To Determine An Overall Diffusion Energy Barrier And An Overall Pre-exponential Factor From The Arrhenius Equation Constructed Through Molecular Dynamics Simulations Of Mean Square Displacement Of The Diffusion Species At Different Temperatures. This Approach Has Been Well Established For Interstitial Diffusion, But Not For Substitutional Diffusion.

Using $In_{0.1}Ga_{0.9}N$ Alloy As An Example, We Have Identified Conditions Where Molecular Dynamics Simulations Can Be Used To Calculate Highly Converged Arrhenius Plots For Substitutional Alloys. It Enables Many Complex Diffusion Problems To Be Easily And Reliably Studied In The Future Using Molecular Dynamics.

INTRODUCTION -

As The Most Pervasive Rate-limiting Mechanism, Diffusion Impacts Almost All The Kinetic Problems Of Materials.

Molecular Dynamics (MD) Simulations Can Be Used To Track The Mean Square Displacements Of Diffusion Atoms And, Hence, Used To Calculate Diffusivities. Diffusivities At Different Temperatures Can Then BeFitted To
The Arrhenius Equation -

$$D = D_0 \exp\ (-Q/kt)$$

to Determine An Overall Diffusion Energy Barrier Q And An Overall Pre-exponential Factor D_0 .But , The Arrhenius Equation Thus Obtained Is Usually Very Noisy. Without Understanding How To Reduce The Statistical Errors, This Method Has Not Been Widely Used Despite Its Many Advantages.

INTRODUCTION -

We Recently Demonstrated That When The MD Simulation Time Is Above 14 ns, The Statistical Error Of The Arrhenius Plot Can Be Reduced To A Negligible Level For InterstiTial Diffusion Such As Hydrogen Diffusion In Aluminium.

- The Much Lower Substitutional Diffusion Rates Are Expected To Result In Larger Statistical Errors Due To The Lack Of Observable Diffusion Events In The Simulations.
- Substitutional Diffusion Cannot Occur Unless There Are Vacancies So That Vacancy Concentration Becomes Another Variable That Has To Be Considered.

The Objective Of The Present Work Is To Provide Researchers With A Good Reference As How MD Methods Can Be Used To Calculate Highly Converged Arrhenius Plots For Substitutional Diffusion, And What Role Vacancies Play In Such Calculations.

METHODS -

$In_{0.1}Ga_{0.9}N$ –

$In_xGa_{1-X}N$ Is Chosen Because It Is An Important Solid-State Lighting Material Whose Properties Can Be Improved Through Control Of Kinetics Of The Synthesis Processes.

LAMMPS Is Used For All MD Simulations Under Periodic Boundary Conditions And A Zero Pressure NPT (Constant Number Of Atoms, Pressure, and Temperature) NOSÈ-HOOVER Thermostat/Barostat.

The Interatomic Forces are Defined by the STILLINGER-WEBER (sw) Potential Format due to its Easy Parameterization for Specific Materials.

Our Intent is to Identify a Method to Extract Accurate Diffusion Properties From a Given Potential.

MELTING TEMPERATURE

- Scale The Simulated Temperature T* to The Real Temperature T Through Homologous Temperature Concept $T = (T^*/T^*_m) \times T_m$

- The Initial wz GaN Crystal Is About

❖ 30 Å In The <1$\bar{1}$00> x Direction ,
❖ 160 Å In The <0001> Y Direction ,
❖ 30 Å In The <11$\bar{2}$0> Z Direction

- The Theoretical Melting Temperature Is Higher Than The Experimental One, $T_m = 2500$ K and the System remains Crystalline at 4100 K.

MELTING TEMPERATURE

- Half Of the Crystal (about 80 Å in the Y-direction) is Melted by First Heating it to 4300 K Over a Period of 8 ns, and Then Equilibrating it At 4300 K for Another 8 ns.
- Finally, the Entire System is Relaxed for a Period of 16 ns Using a Zero Pressure Isenthalpic NPH (Constant Number Of Atoms, Pressure, And Enthalpy Dynamics)
- The Melting Temperature Is Calculated As The Time-averaged Temperature In The Final 8 ns Period .
- We find $T^*_m = 3570 \pm 1$ K Where The Error Was Estimated From 3 Independent MD Simulations.

DIFFUSIONS SIMULATIONS

1) Initial calculations :

- t = 1.0 ns ($\Delta t = 0.004$ ns),
- T* = 2500–2900 K ($T^* / T_m^* = 0.70–0.81$),
- Vacancy Concentration of Cv = 5%

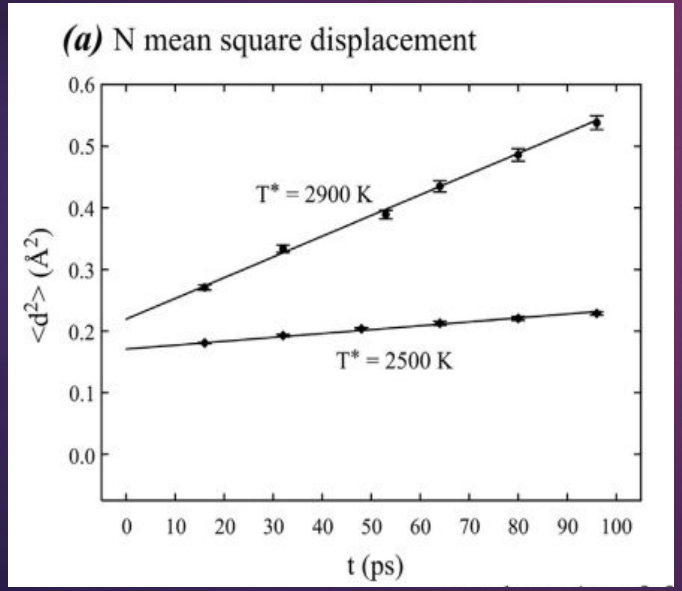

Fig. 1(a) appears to Show The Expected Linear Relationship Between Mean Square Displacement And Time

Atomic Vibration Always Gives A Finite Mean Square Displacement Even When The Atoms Have Not Made Any Jumps (i.e., The Mean Square Displacement From Diffusion Is conceptually zero at this time). Due To This Thermal Vibration, Our Calculated Mean Square Displacement Does Not Have A Zero Intercept

DIFFUSIONS SIMULATIONS

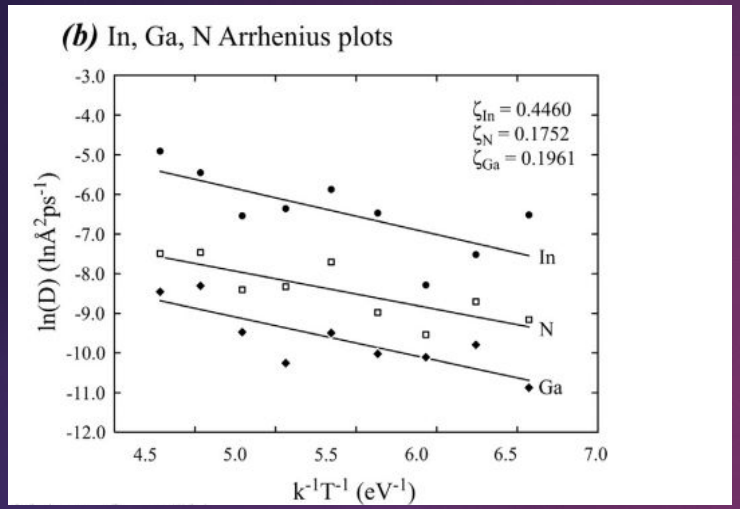

Fig. B) Indicates Significant Noise For The Arrhenius Plots.

The Statistical Noise Can be Quantified by the Mean Square Deviation of the Fitted Arrhenius Equation from the MD Data points

- The Values For Mean Square Deviation Error Parameter Are Above 0.15 For In, Ga, And N , which Is Way Above The Satisfactory Levels Of 0.008
- Therefore , Due to The large Statistical Error shown in fig. 1(b), Accurate Diffusion Energy Barriers And Pre Exponential Factors cannot be Extracted.

DIFFUSIONS SIMULATIONS

2) Effects of Time :

- $T^* = 3100–3500$ K ($T^*/T^*_m = 0.87–0.98$),
- Vacancy Concentration of $C_V = 5\%$,
- Various Simulation Time t Between 0.5 and 1000.0 ns ($\Delta t = 0.004$ ns for $t \leq 20.0$ ns, and $\Delta t = 0.1$ ns for $t > 20.0$ ns)

DIFFUSIONS SIMULATIONS

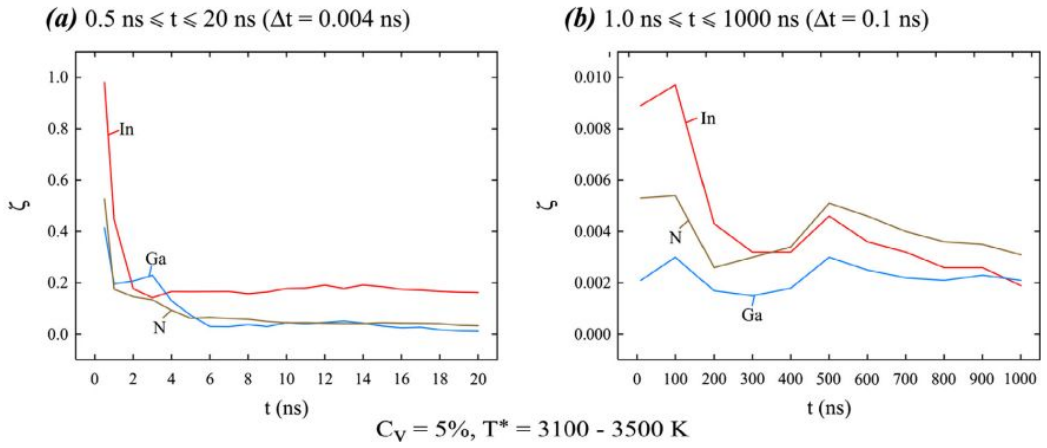

Fig. 2. Error parameter ζ for Arrhenius fits as a function of time for (a) 0.5 ns ⩽ t ⩽ 20.0 ns (Δt = 0.004 ns) and (b) 1.0 ns ⩽ t ⩽ 1000.0 ns (Δt = 0.1 ns). Temperature range $T^* = 3100–3500$ K ($T^*/T^*_m = 0.87–0.98$), and vacancy concentration $C_V = 5\%$.

Errors At t = 10 ns seem To Be smaller in fig. 2 (b) than in fig. 2(a), Suggesting that a large Δt may help improve the convergence.

Large Δt Can Only Be Used When Total Simulation Time T Is Much Larger. Fig. 2(b) Extends The Total Simulation Time To 1000.0 Ns At A Relatively Large Δt Of 0.1 Ns. These Time Scales Are Much Longer Than Those We Used For Interstitial Diffusion Where T = 10 Ns Seems To Produce Satisfactory Results. This Is Intended Because We Want To Provide A Good Reference For Future Researchers To Determine Appropriate Time To Perform Substitutional Diffusion Calculations, Especially Considering That Such Calculations Are More Difficult To Converge.

DIFFUSIONS SIMULATIONS

3) Effects of Temperature Range :

- Vacancy Concentration of C_V = 5%,
- Simulation Time of t = 10.0 ns (Δt = 0.004 ns)
- Two Temperature Ranges of T*= 2500–2900 K (T^*/T^*_m = 0.70–0.81) and T* = 3100–3500 K (T^*/T^*_m = 0.87–0.98)

DIFFUSIONS SIMULATIONS

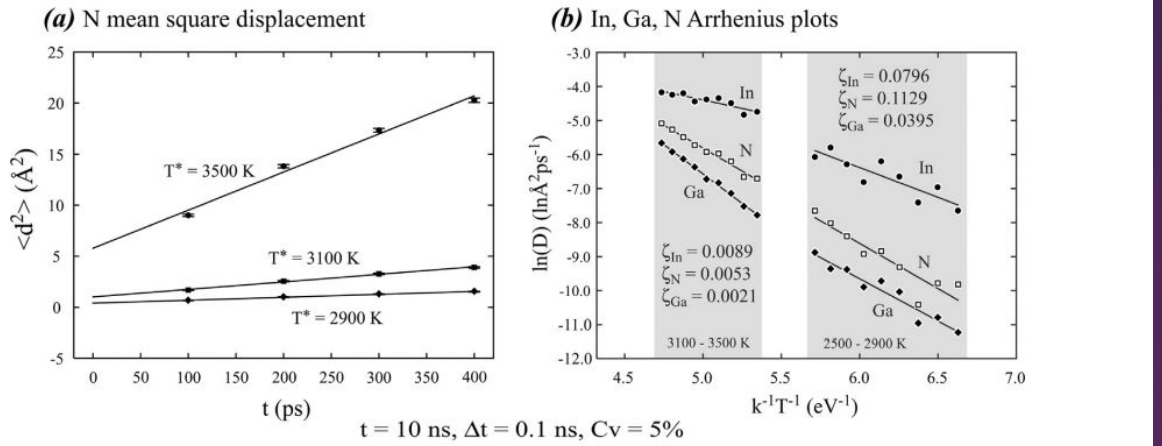

Fig. 3. (a) Mean square displacement of N and (b) In, Ga, and N Arrhenius plots obtained at a vacancy concentration of $C_V = 5\%$, a simulation time of t = 10.0 ns, and two temperature ranges of $T^* = 2500–2900$ K ($T^*/T^*_m = 0.70–0.81$) and $T^* = 3100–3500$ K ($T^*/T^*_m = 0.87–0.98$).

Fig. 3(a) confirms the linear relationship between the mean square displacement and time.

Fig. 3(b) indicates that the Arrhenius plots obtained for the higher temperature range are more converged than those obtained for the lower temperature range.

The Lack of Convergence at the Lower Temperature Range is also manifested by the Discontinuity of the Plots between the Two Temperature ranges. The more converged results at the higher temperature is again understandable because more diffusion events are sampled at higher temperatures

DIFFUSIONS SIMULATIONS

4) Effects of Vacancy Concentration:

- Simulation Time of t = 10.0 ns (Δt = 0.1 ns)
- Temperature Ranges of T^*= 3100–3500 K (T^*/ T^*_m = 0.87–0.98)
- Two Vacancy Concentration of C_V = 1%, and C_V = 5%,

DIFFUSIONS SIMULATIONS

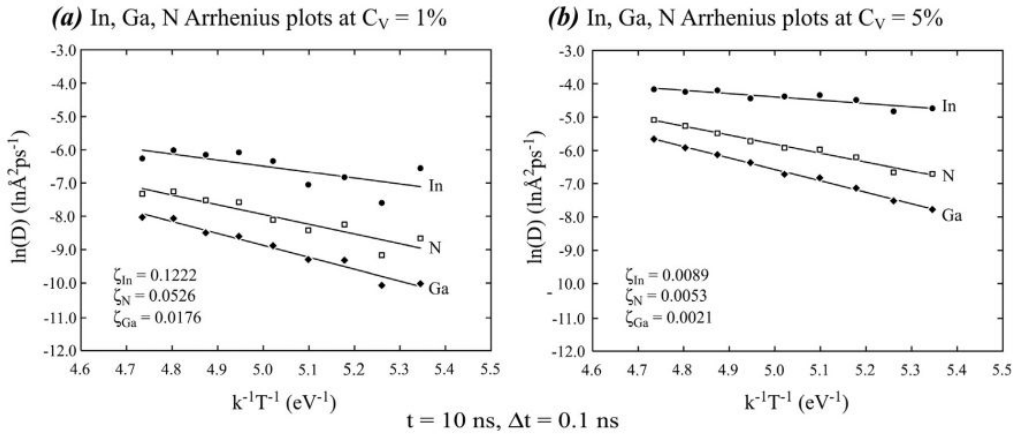

Fig. 4. In, Ga, and N Arrhenius plots at (a) a vacancy concentration of C_V = 1% and (b) a vacancy concentration of C_V = 5%. Temperature range T^* = 3100–3500 K (T^*/T^*_m = 0.87–0.98), and simulation time t = 10.0 ns.

The In, Ga, N Arrhenius plots constructed for C_V = 1% and C_V = 5% are shown respectively in Fig. 4(a) and (b)

The diffusivities obtained for the lower vacancy Concentration are lower than the diffusivities obtained at the higher vacancy concentration. Because substitutional diffusion must proceed through the vacancy migration mechanism

Zero Diffusivities Are Obtained At The Zero Vacancy Concentration
The Higher Vacancy Concentration Seems To Give Smaller Statistical Errors, Which Is Reflected By The F Values Marked In The Figures. This Is Again Because A Higher Vacancy Concentration Registers More Diffusion Events In The Simulations

DIFFUSIONS SIMULATIONS

5) Converged Calculations

High Temperature Range Such As T^*/T^*_m = 0.87–0.98 And A Long Simulation Time Such As T = 1000.0 ns Lead To Converged Arrhenius Plots For Substitutional Diffusion. We Therefore Calculate Diffusion Properties For $In_{0.1}Ga_{0.9}N$ Samples With Various Vacancy Concentrations C_v = 0.0, 0.1, 0.2, ..., 0.5 Using T^*/T^*_m = 0.87–0.98 And T = 1000.0 Ns. We Then Fit All The Data To The Arrhenius Equation Assuming That The Activation Energy Depends Only On Diffusion Species Whereas The Pre-exponential Factor Depends On Both Diffusion Species And Vacancy Concentration. The Fitted Results Are Summarized In Table 1.

Table 1
Diffusion energy barrier Q (eV), pre-exponential factor D_0 (Å^2/ps), and error of Arrhenius fit ζ for In, Ga and N at different vacancy concentrations C_V, obtained using T^*/T^*_m = 0.87–0.98 and t = 1000.0 ns.

C_V (%)	In			Ga			N		
	Q	D_0	ζ	Q	D_0	ζ	Q	D_0	ζ
0	No diffusion detected								
1	1.365	1.454	0.0068	3.443	4299.05	0.0032	2.681	236.96	0.0053
2		3.886			12293.30			631.67	
3		5.741			20241.40			981.01	
4		8.424			30450.50			1463.95	
5		11.465			42223.30			2032.25	

DIFFUSIONS SIMULATIONS

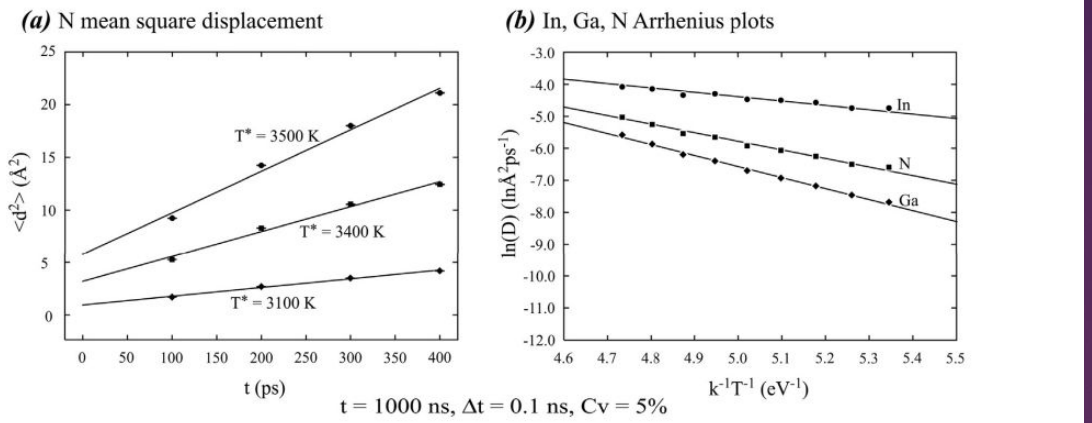

Fig. 5. (a) Mean square displacement of N and (b) In, Ga, and N Arrhenius plots obtained at a temperature range of $T^* = 3100–3500$ K ($T^*/T_m^* = 0.87–0.98$), a vacancy concentrations of $C_V = 5\%$, and a simulation time of t = 1000.0 ns.

The mean square displacements and arrhenius plots for typical examples are shown respectively in fig. 5(a) and (b)

Using nitrogen diffusion at a few temperatures and C_V = 5% as examples ig. :

5(a) Verifies that the linear Relationship Between Mean Square Displacement and Time is Well satisfied. Using C_V = 5% as an example, Fig. 5(b) confirms an Excellent Convergence to the linear Arrhenius plots for In, Ga, and N diffusion. This justifies our assumption that Diffusion energy Barrier is Insensitive to Vacancy Concentration (C_V).

DIFFUSIONS SIMULATIONS

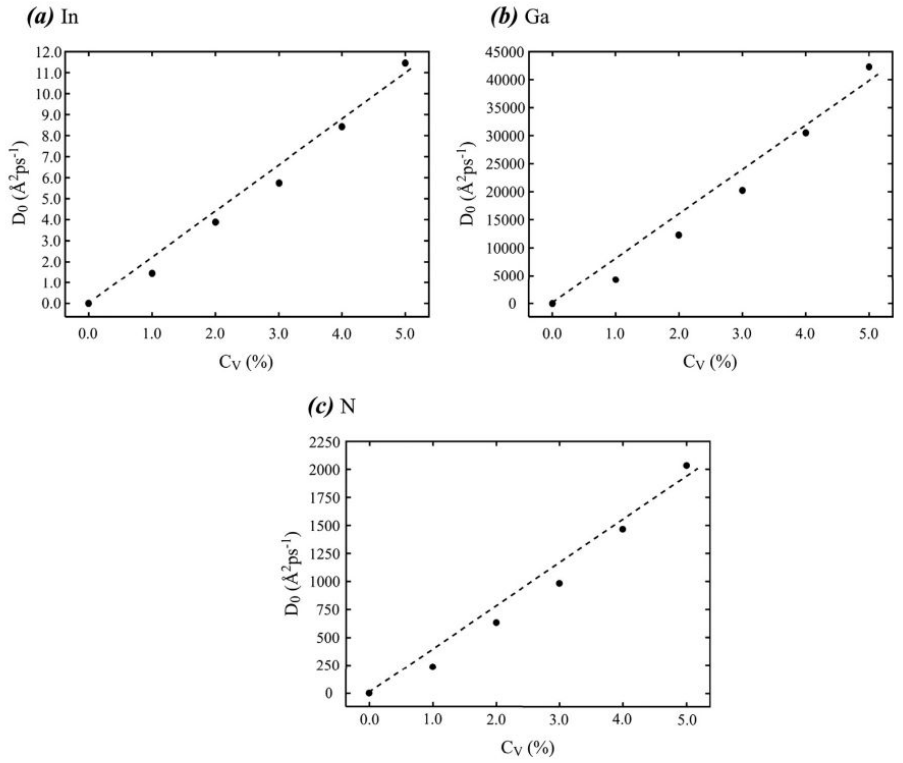

Fig. 6. Pre-exponential factors as a function of vacancy concentration for (a) In; (b) Ga; and (c) N. The dash lines are used to guide eyes and are not fits.

Fig. 6. Pre-exponential factors as a function of vacancy concentration for (a) In; (b) Ga; and (c) N

The Results Demonstrated In Figs. 5 And 6 Strongly Indicate That Highly Converged Diffusion Energy Barrier And Preexponential Factor For Substitutional Diffusion Can Be Obtained By Fitting To Md Diffusivities Obtained At Different Temperatures And Vacancy Concentrations

CONCLUSIONS :

- Molecular Dynamics Simulations Have Been Explored To Extract Overall Energy Barriers And Pre-exponential Factors For Substitutional Diffusion From Arrhenius Equations. We Find That Highly Converged Results Can Be Obtained When Using An Elevated Temperature Range (e.g. $T^*/T^*_m = 0.87–0.98$), An Extended Simulation Time And Various Vacancy Concentrations Between 1% And 5%.

- In The Dilute Limit, Increasing Vacancy Concentration Linearly Increases The Preexponential Factor, But Does Not Impact The Diffusion Energy Barrier. The Observed Improvement Of Convergence Due To Increased Temperature, Time, And Vacancy Concentration Can All Be Attributed To Increased Sampling Of Diffusion Events During Simulations.

- In Addition To Provide A Robust MD Method To Simulate Substitutional Diffusion, Our Results Also Prove That With The Help Of Vacancies, Molecular Dynamics Simulations Can Be Used To Equilibrate Atomic Populations In Substitutional Lattices.

REFERENCES :

Molecular Dynamics Simulations Of Substitutional Diffusion

BY - X.W. Zhou , R.E. Jones, J. Gruber
Sandia National Laboratories, USA

https://www.sciencedirect.com/science/article/pii/S0927025616306085

THANK YOU

Solute partition at solid-liquid interface of binary alloy from molecular dynamics simulation

By- Pradumn Patidar (190005030)

Abstract

Molecular dynamics simulations are performed to calculate the solute partition at the solid–liquid interface of binary alloy. Solidus and liquidus compositions are directly derived from the equilibrium composition and it is directly confirmed from the simulation that the propagation velocity of the solid–liquid interface with solute partition is much smaller than that of the partitionless solidification.

However, It is significant in this study to present a simple approach of the estimation of partition-based properties including interfacial dynamics since it is not straightforward for conventional Monte-Carlo simulations to treat the solute partition and the interfacial dynamics simultaneously.

Introduction

1. Since many practical metallic materials are produced via solidification, it is essential to control the solidification microstructure to obtain products with desired properties. It is well known that solid–liquid interfacial properties strongly affect the solidification microstructure.
2. In this study, we present a simple approach to calculate solute partition-based properties of the solid–liquid interface from the MD simulation. In particular, solidus and liquidus compositions are directly estimated by monitoring the equilibrium composition at the solid–liquid interface of the binary alloy.

Introduction

3. Then, the effect of solute partition on the propagation velocity of the solid–liquid interface is closely discussed. Here, Fe–Cr alloy is examined as a model case, in which the partition coefficient changes significantly between Fe-rich and Cr-rich composition.

4. As a practical methodology for this problem, composition ratio of a binary alloy with respect to the chemical potential difference can be estimated using the semi-grand canonical Monte-Carlo (SGCMC) simulation for a given interatomic potential.

Simulation details

- Molecular Dynamics simulations were carried out using the LAMMPS software and the EAM (embedded atom method) potential fitted by Bonny et al. is employed as the interatomic potential for the Fe–Cr alloy, which is fitted for thermodynamic and point-defect properties obtained from experiments and density functional theory (DFT) calculations.
- The parameter files for the EAM potential are taken from the database of NIST– IPR (Interatomic Potential Repository) project are utilized for the MD simulation by the LAMMPS.

- The velocity-Verlet method is used to integrate the classical equation of motion with a time step of 1.0 fs. The Nose–Hoover thermostat and barostat are employed to control temperature and pressure.
- The OVITO (open visualization tool) is used for the visualization of simulation results.
- Solid–liquid biphasic systems are employed for the estimation of melting points for pure metals (Fe and Cr) and the investigation of interfacial properties of the Fe–Cr alloy.
  - For pure Fe and Cr, two bcc crystals consisting of (125,000 atoms) are analyzed.

Creating simulation Model

- For alloys, consisting of (93,750 atoms) with the target concentration are annealed for 10 ps with the NVT (number of atoms, volume and temperature)– constant ensemble to obtain solid and liquid structures, respectively.
- Then, these structures are connected with the (100) plane appearing on the interface and the energy minimization is performed to avoid the unexpected proximity of atoms at the solid–liquid interface.
  - Prior to the estimation of the solute partition-based properties of Fe–Cr alloy, melting points of pure Fe and Cr for the EAM potential employed in this study are estimated by the convergence temperature technique.

Some more points on simulation model

- Solid–liquid biphasic systems of pure Fe and Cr are employed with the NPT ensemble for 25 ps at 1700, 1750 and 1800 K for Fe and at 2600, 2650 and 2700K for Cr, respectively.
- Then, the systems are relaxed with the NPH (number of atoms, pressure and enthalpy)–constant ensemble for subsequent 1975 ps. The pressure is maintained at 0 Pa in all processes.
- Melting points of Fe and Cr for the EAM potential with Bonny's fitting are estimated to be 1770±10 K for Fe and 2670±10 K for Cr, respectively.
  - The melting point of Fe for the EAM potential employed in this study is close to the experimental value(~1811K) ,whereas that of Cr is approximately 20% higher than the experimental value.

- Next, solidus and liquidus compositions with respect to temperature are estimated. The solid–liquid biphasic system of the Fe–Cr alloy with homogeneous composition is used with the NPT ensemble.
- For the Fe-rich Fe–Cr alloy (19.1at%Ct and less), the NPH ensemble is employed. Calculations are carried out until the propagation of the solid–liquid interface does not proceed.
- Then, the convergence compositions at the interface are regarded as the equilibrium compositions of solid and liquid phases at the set temperature.

Results and Discussion

Extraction of Solidus-Liquidus Composition

1. The solid–liquid interface propagates only about ~40Å after the 3000 ps calculation.In both cases, solidification happens at the initial stage and the solid– liquid interface propagates toward the liquid phase.
2. The propagation of the interface stops after approximately 12,000 ps and the distribution of Fe composition becomes constant.
3. Solidus and liquidus compositions are estimated from the convergence compositions to be 7% and 14% at 2500 K and 12% and 23% for 2400 K, respectively.
4. On the other hand, the significant solute partition is not observed at the Fe-rich composition (at 19.1% or less).

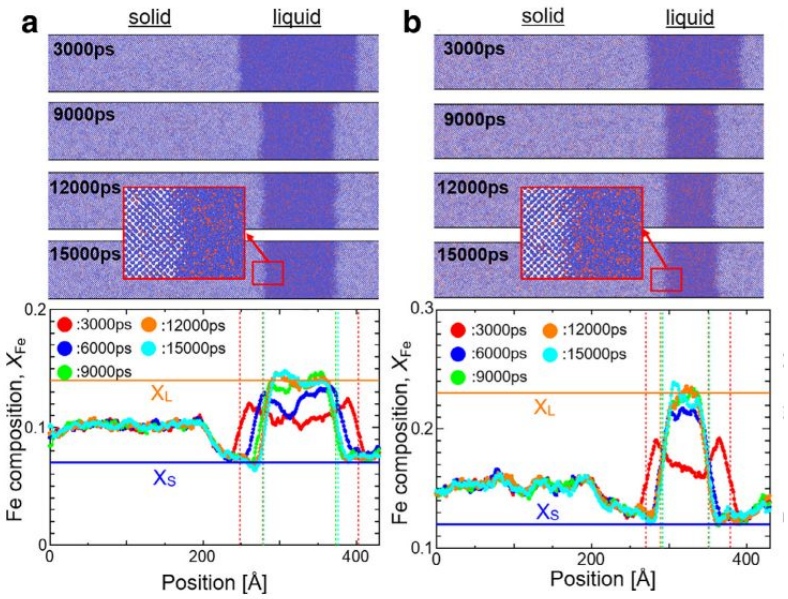

Fig. 1(a) and (b) show the snapshots and the distributions of Fe composition consisting of solid–liquid biphasic system (a) Fe-90%Cr at 2500 K and (b) Fe-85%Cr at 2400 K.

Calculating equilibrium temperature

- The migration of solute-liquid interface after 3000 ps is (~20Å) after that there is not significant change in the solute distribution till the 15,000 ps calculation.
- Finally, the system temperature is converged to be 1773 K, which is regarded as the equilibrium temperature for Fe-10%Cr alloy at the EAM potential employed in this study.

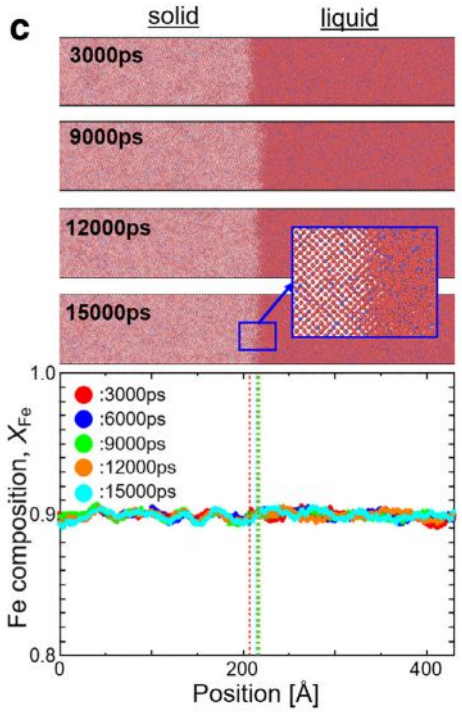

Fig. (c) Fe composition for the solid–liquid biphasic system of Fe- 10%Cr (temperature not controlled).

The phase diagram of Fe–Cr alloy

1. Phase diagram of Fe–Cr alloy for the EAM potential derived from the MD simulation.
2. compositions of the miscibility gap at low temperature are plotted for reference, which are quoted from the semi-grand canonical Monte-Carlo(SGCMC) simulation by Bonny et al.
3. The solute partition happens at Cr-rich concentration, whereas the solute partition is not critical at the Fe-rich composition

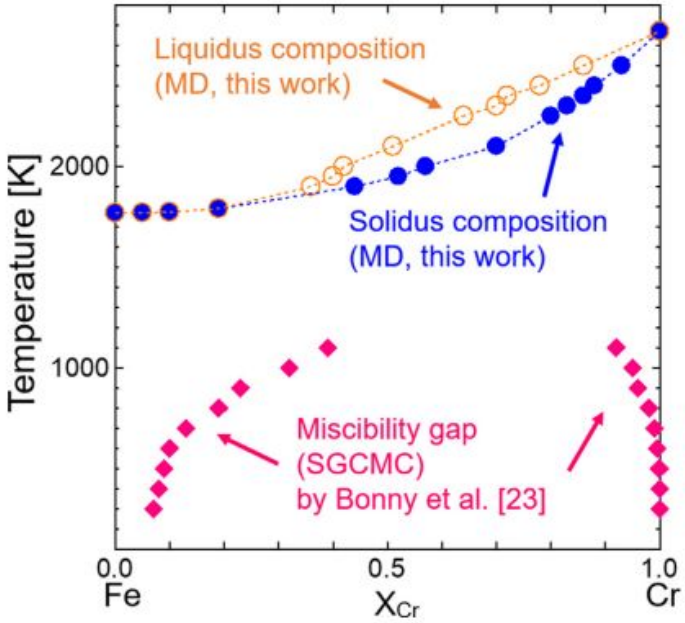

The phase diagram of Fe–Cr alloy.

Interfacial composition analysis

1. In the case of the 2200 K, the Fe concentration at the newly-solidified solid region becomes lower than that at the same position before the solidification.
2. The solid–liquid interface propagates only about 50 Å after the 15,000 ps calculation. On the other hand, the distribution of the Fe composition does not change during the solidification at 2050 K, which means the solute trapping happens during the solidification.
3. In this case, all liquid region is solidified within at approximately 500 ps, which is much faster than the case of 2200 K

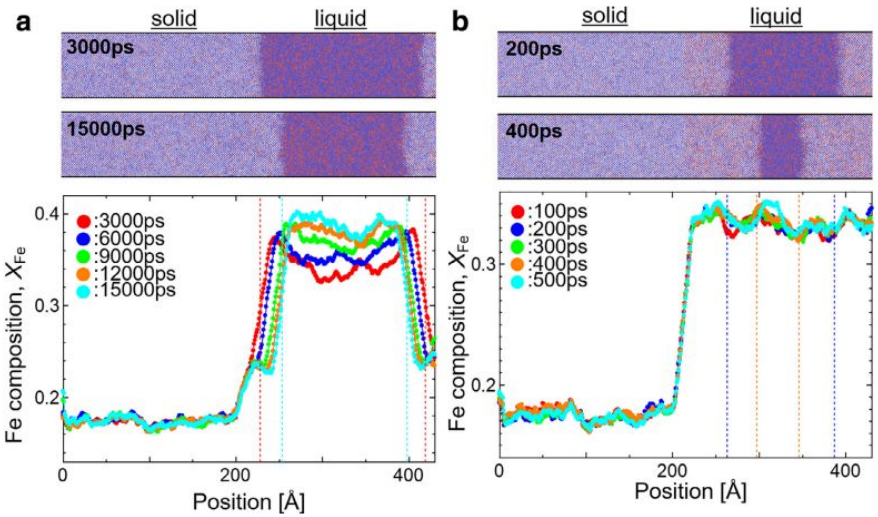

Fig. shows Snapshots and the distribution of Fe composition for the solid–liquid biphasic system consisting of Fe-83%Cr solid and Fe-67%Cr liquid during the relaxation at (a) 2200 and (b) 2050 K, respectively

4. Therefore, the solute partition hinders the propagation of solid– liquid interface in the case of the temperature near the equilibrium temperature.
5. On the other hand, the interfacial velocity of the partitionless solidification is much faster than that of the solidification with solute partition.

Propagation velocity & Kinetic Coefficient Estimation

The propagation velocity of the interface in this system is closely examined between 2000 and 2550 K at 50 K interval.

1. Near the equilibrium temperature, the change in velocity with respect to temperature is very small, whereas that becomes larger when the temperature is away from the equilibrium.
2. The slope of the propagation velocity with respect to temperature T is known to be the kinetic coefficient. $V = \mu(T_{eq} - T),$
3. kinetic coefficients Fe-83%Cr (solid) and Fe-67%Cr (liquid) are 0.178, and 0.132 m/sK, respectively.

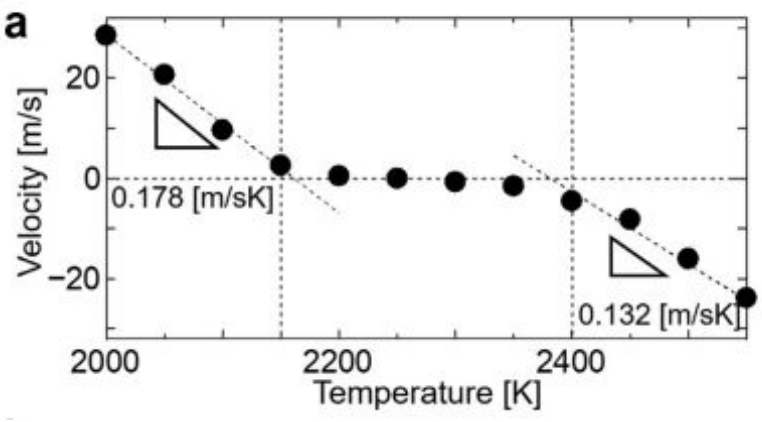

Fig. (a) shows the propagation velocity of the solid–liquid interface as a function of temperature for the biphasic system of a Fe-83%Cr (solid) and Fe-67%Cr (liquid)with the equilibrium composition at 2300 K.

1. In this case, there is no region with a small slope and the velocity is changing monotonically with respect to temperature difference.
2. From the slope, the kinetic coefficient is estimated to be 0.178 m/sK, which is close to that for partitionless solidification in Fe-83%Cr (solid).
3. Therefore, the kinetic coefficient of the partitionless solidification for the binary alloy is considered to be the order of 0.1 m/sK.

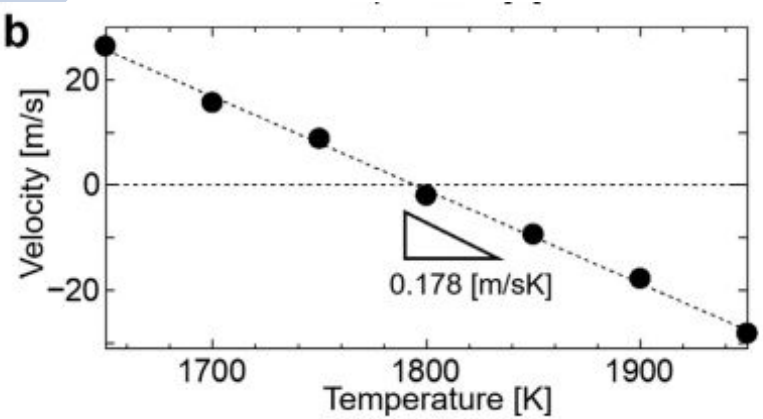

Fig. (b) shows the propagation velocity of the solid–liquid interface as a function of temperature for the biphasic system of Fe-19.1%Cr.

Conclusion

We have obtained solute partition-based properties of the solid–liquid interface of the Fe–Cr alloy from the MD simulation. Especially, solidus and liquidus compositions are successfully derived from the equilibrium composition at the solid–liquid interface. Moreover, the composition dependence on the propagation behavior of the solid–liquid interface is investigated.

1. It is revealed that the solute partition hinders the propagation of solid– liquid interface in the case of the temperature near the equilibrium temperature.
2. On the other hand, diffusion is not dominant during the partitionless solidification, at which the temperature effect is the dominant.
3. From the Simulation data, the kinetic coefficient of the partitionless solidification for the binary alloy is considered to be the order of 0.1 m/sK.

Reference

- Solute partition at solid-liquid interface of binary alloy from molecular dynamics simulation.
  Kensho Ueno, Yasushi Shibuta
  https://www.sciencedirect.com/science/article/abs/pii/S2589152918301996

Thank You

Molecular dynamics simulations of wetting behavior of water droplets on polytetrafluorethylene surfaces

Ayush Nath
190005009

1. Introduction

Polytetrafluoroethylene (PTFE)

Polytetrafluorethylene (PTFE) is a widely used engineering material in aviation, mechanics, and other fields, especially because of its hydrophobicity. The nanostructure of the solid surface has an important influence on its hydrophobicity. In addition, because of the interest in designing microfluidic systems, the nano-wetting properties of surfaces are attracting increasing attention.

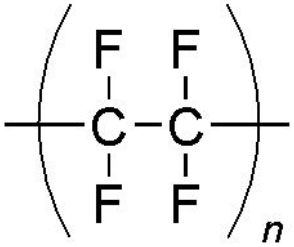

Structure of PTFE polymer

Aim

This paper aims to :-

1. Study the effect of cutoff on the contact angle of the flat surface and the variation trend of the contact angles.
2. Investigate the differences between the two equilibrium states and the reasons why cross contact exists. This research is significant for studying the characteristics of the water–solid interface, including the wettabilities of different nanostructured surfaces.

2. Methods for Simulation

Model set-up

Simulation Model

For the simulations, a model composed of a cubic box of water molecules located on the solid surface was constructed.

The water model in this study was the rigid extended simple point charge potential (SPC/E). The charges on the oxygen and hydrogen atoms were −0.8476e and +0.4238e. The O–H distance was 1 Å and the H–O–H angle was 109.47°.

1. The number of water molecules in a single layer was 400.
2. Flat and pillar surfaces of PTFE were considered as the solid surfaces.
3. The model of the flat surface is referred to as the planar crystal model. A planar zigzag structure with density 2.101 g/cm3 and a layer with 36 chains of $[CF2CF2]_{100}$ served as the model of the flat PTFE surface.
4. The charge on a carbon atom was +0.5500e and the charge on a fluorine atom was -0.2750e.

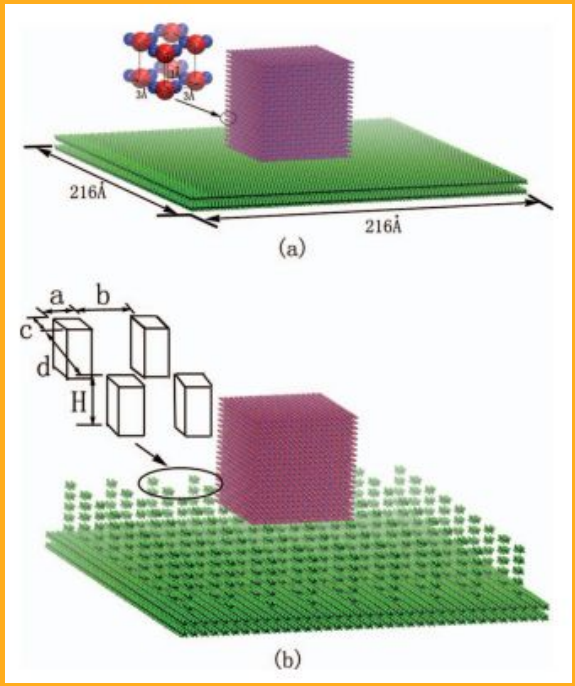

FIG. 1. Initial structures of the ensembles of (a) the flat surface and (b) the pillar surface. Blue, red, black, and green spheres represent the hydrogen, oxygen, carbon, and fluorine atoms, respectively.

Some more info on simulation model

The model of the pillar PTFE surface consisted of two parts: the substrate and the pillars. The model of the substrate was the same as the flat PTFE surface and pillars were cut from the flat surface (Figure 1(b)).

For comparison, similar simulations of the pillar surfaces with different pillar dimensions were carried out. The pillar surfaces were named P1, P2, P3, and P4, which were based on the dimensional parameters of the pillars (Table I). f is the ratio of the pillar area to the whole area per unit:

The dispersion and repulsion forces were modeled using the Lennard–Jones (LJ) potential Eq (2):

In this equation, i and j are carbon (C), oxygen (O), fluorine (F), and hydrogen (H) atoms. σ_{ij} and ε_{ij} are the distance where the interatomic potential is zero and the depth of the potential well, respectively.

	a (Å)	b (Å)	c (Å)	d (Å)	H (Å)	f
P1	5.9	18.1	7.4	16.5	30	7.6%
P2	11.8	11.6	14.7	11.0	30	28.9%
P3	18.3	6.9	20.8	5.6	30	57.2%
P4	5.9	6.9	7.4	5.6	30	26.3%

TABLE I. Dimensional parameters for the periodic pillar structures on the PTFE surface.

$$f = \frac{a \times c}{(a+b) \times (c+d)} \times 100\%. \quad (1)$$

$$U_{ij} = 4\varepsilon_{ij}\left[\left(\frac{\sigma_{ij}}{r_{ij}}\right)^{12} - \left(\frac{\sigma_{ij}}{r_{ij}}\right)^{6}\right] \quad (2)$$

MD Simulation using Lammps package

The mixed-atom interatomic potentials were obtained through the Lorentz–Berthelot mixing rules Eq (3), (4)

$$\sigma_{ij}=\tfrac{1}{2}(\sigma_{ii}+\sigma_{jj}) \qquad (3)$$

$$\varepsilon_{ij}=(\varepsilon_{ii}\varepsilon_{jj})^{1/2} \qquad (4)$$

The electrostatic interaction was modeled using Coulomb's law, and the PPPM method was applied to minimize the errors in the long-range interactions. The lateral size of the simulation cell was four times the length of the water cube, and the influence of molecules in duplicate domains on droplets could be ignored. All simulations were carried out in the NVT (fixed number of particles, volume, and temperature) ensemble at T = 300 K for 1 ns with an integration time step of 1 fs. The SHAKE algorithm was used to keep the O–H distance fixed at 1 Å and the H–O–H angle fixed at 109.47°. The atoms of PTFE were fixed at their initial positions and represented an inert wall. After 200 ps equilibration time, samples of the trajectories were stored every 100 ps. During the production run, the water temperature remained stable at 300 K with deviation less than 5.0 K.

3. Results and Discussion

Extracting the contact angle values

From the MD simulation trajectories, the 3D coordinates of every atom at each moment could be obtained. To extract the contact angle from the coordinates, a two-step procedure was adopted.

1. Graph of atomic positions drawn in the x-z plane
2. Circular best fit through these points was extrapolated to the solid surface where the contact angle was measured

To determine the effect of the cutoff on the contact angle, three cutoffs (9, 12 and 15 Å) were used. The distance between the bottom of water droplet and the bottom of PTFE substrate was 15.3 Å, which is larger than the largest cutoff. If the thickness of the substrate increases, the distances between the water molecules and PTFE atoms in the additional part are larger than the cutoff, and interactions between them could be ignored. Therefore, the thickness of the PTFE model is suitable and not thinner than the cutoffs studied.

Variation of contact angle with water droplet size for different cutoffs

The results in Figure 2 show that the sensitivity of the contact angle to the number of water molecules is low. The contact angle at a cutoff of 9 Å changed from 98° to 103°, which is a small variation. This phenomenon was similar for the other two cutoffs. Increasing the cutoff increases the simulation accuracy, as well as increasing the simulation time.

An appropriate cutoff is important for simulations. The cutoff mainly affects the action range of the LJ potential, According to Eq. (2), the potential energy is the sum of LJ potentials and can be represented as we can see on the right Eq (5). The total potential energy and cutoff energy are calculated, which are called E_{total} and $E_{r>cutoff}$, respectively. Considering some conditions, we get the values of b constant as ∞ for both energies. the value of a for the total potential energy of E_{0-0} was set at 2.8 Å.

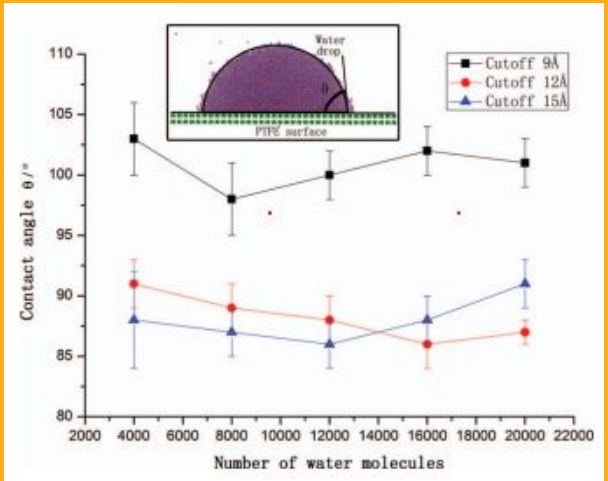

FIG. 2. Variation of the contact angle with water droplet size for different cutoffs

$$E = \int_a^b \rho \times \frac{4\pi r^2}{M} \times Na \times 4\varepsilon \left[\left(\frac{\sigma}{r}\right)^{12} - \left(\frac{\sigma}{r}\right)^{6} \right] dr \quad (5)$$

Selecting the cutoff for simulation

The proportion of $E_{r>cutoff}$ in E_{total} has also been analyzed, and is defined as ω Eq. (6). The results from the theoretical calculation have been listed in Table 2.

1. Deviation of the potential energy at a cutoff of 9 Å is as high as 9.93%.
2. The effect of cutoff on the simulated results could be indirectly reflected by the deviation of the potential energy.
3. To obtain an appropriate cutoff for the simulations, calculations of potential energy can be used.
4. Deviations decreased to ~2% when the cutoff was increased to 15 Å.
5. The contact angles of the flat surface simulated at a cutoff of 15 Å were near 90° and no well-defined linear fit with droplet size was observed.

$$\omega\% = \frac{E_{r>cutoff}}{E_{total}} \times 100\%. \quad (6)$$

	Cutoff (Å)	$E_{r>cutoff}$ (kcal)	E_{total} (kcal)	ω%
O–O	9	1.35×10^{29}	1.36×10^{30}	9.93%
O–O	12	5.71×10^{28}	1.36×10^{30}	4.20%
O–O	15	2.92×10^{28}	1.36×10^{30}	2.15%
C–O	9	1.36×10^{29}	1.37×10^{30}	9.92%
C–O	12	5.73×10^{28}	1.37×10^{30}	4.19%
C–O	15	2.93×10^{28}	1.37×10^{30}	2.14%
F–O	9	6.67×10^{28}	1.08×10^{30}	6.19%
F–O	12	2.82×10^{28}	1.08×10^{30}	2.61%
F–O	15	1.44×10^{28}	1.08×10^{30}	1.34%

Table 2. Total potential energy and cutoff energy at different cutoffs

Simulated contact angles for different PTFE surfaces (P1, P2, P3, P4)

The table on the right gives us an idea on how the contact angles varied on different PTFE surfaces. Some of the results which we infer from the data:-

1. The contact angles of the pillar surfaces varied from 87° to 115°, and the values were larger than those of the flat surface.
2. This indicated that the hydrophobicity increased on the rough surfaces.
3. The different pillar structures resulted in two different equilibrium wetting geometries.
   a. Wetted contact state
   b. Cross contact state

Type of PTFE surface	Number of water molecules	Contact angle (deg)	Deviation (deg)
	$A = \infty$, $f = 100\%$		
Flat	8000	87	1
Flat	12000	86	2
Flat	16000	88	1
Flat	20000	91	2
	$A = 43.7$ Å^2, $f = 7.6\%$		
P1	8000	91	2
P1	12000	100	3
P1	16000	108	2
P1	20000	111	2
	$A = 173.5$ Å^2, $f = 28.9\%$		
P2	8000	87	5
P2	12000	101	4
P2	16000	112	2
P2	20000	115	2
	$A = 380.6$ Å^2, $f = 57.2\%$		
P3	8000	95	2
P3	12000	95	2
P3	16000	96	3
P3	20000	93	3
	$A = 43.7$ Å^2, $f = 26.3\%$		
P4	8000	104	3
P4	12000	105	3
P4	16000	105	1
P4	20000	106	2

Table 3. Simulated contact angles for different numbers of water molecules on the PTFE surface

Equilibrium states on the different PTFE surfaces (P1, P2, P3, P4)

The different equilibrium states with 12 000 water molecules are shown in Figure 3. Some of the results inferred are :-

1. The results show that the P1 and P2 surfaces were fully wetted by water molecules, while the P3 and P4 surfaces were not.
2. The decrease of distances caused changes in the contact type. The distances between pillars of the P1 and P2 surfaces were two to three times larger than that of the P4 surface.
3. Therefore, the hollows were large enough to accommodate numerous water molecules, which led to wetted contact.
4. Confined water molecules prevented other molecules above the surface from penetrating into the hollows, which resulted in cross contact.

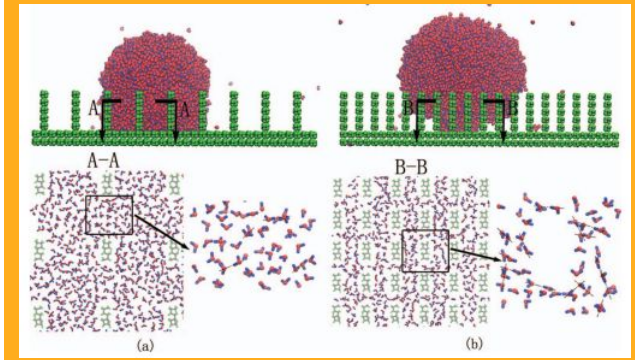

Fig. 3. Snapshots of equilibrium states for (a) the P1 surface (wetted contact) and (b) the P4 surface (cross contact, top panel). The locations and bond orientations of confined water molecules are shown in the bottom panel. The blue and red spheres represent hydrogen and oxygen atoms, respectively. Dotted dashed lines are drawn to indicate the OH bond pointing towards the oxygen atom of its neighbor molecule.

Variation of contact angle for droplet size for flat, P1, P2 surfaces of PTFE.

Results inferred :-

1. The value of the contact angle is dependent on the size of the droplet for the wetted contact.
2. Also shows that the contact angle increases with increasing droplet size.
3. It also revealed that the contact angle of the P2 surface was always larger than that of the P1 surface for the same sized droplet.
4. For a same sized water droplet, the droplet left a larger volume of liquid between pillars of the P1 surface because the volume of the hollows on the P1 surface was larger than that on the P2 surface.
5. The water formed a smaller droplet above the P1 surface, which resulted in a smaller contact angle.

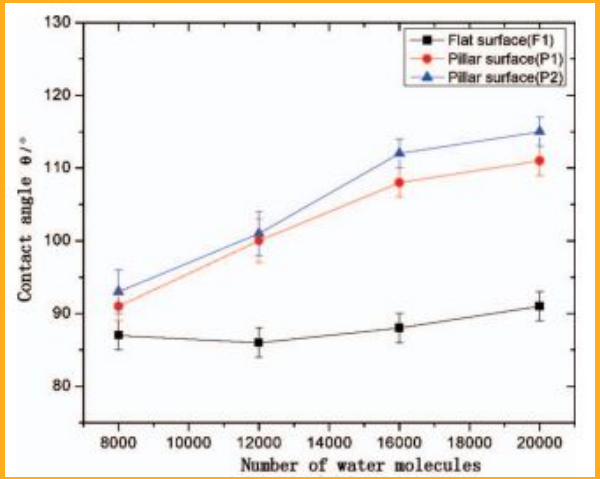

FIG. 4. Variation of the contact angle with water droplet size for flat, P1, and P2 surfaces

Variation of contact angle for droplet size for flat, P3, P4 surfaces of PTFE.

The results of the P3 or P4 surfaces (Fig 5) show that :-

1. Contact angle of different droplet sizes remain stable
2. Contact angles of cross contact had weak sensitivity to the droplet sizes.
3. For the same sized droplet, the contact angle of the P3 surface is larger than that of the flat surface and smaller than that of the P4 surface.
4. The increase of contact angles from P3 surface to P4 surface could be seen to follow the decrease in the contact area of the liquid with the solid

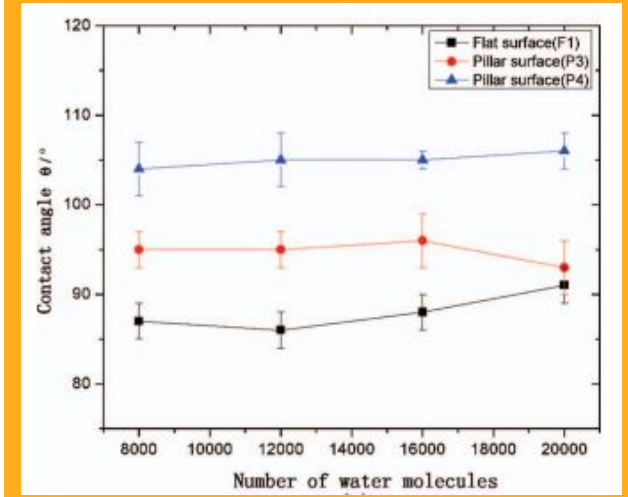

Fig. 5. Variation of the contact angle with water droplet size for flat, P3, and P4 surfaces

Is the cross contact state stable?

To determine if the cross contact state is a stable state or not, additional simulations were carried out.

1. To verify whether the cross state was fully stabilized at 1 ns, the simulation time was extended to 3 ns. Results were the same at 3ns which proves 1ns is sufficient.
2. Next a wetted P3 model with 12 000 water molecules was simulated, in which the water molecules were initially placed between pillars (Figure 6(a-i)).
3. A new water model with same 12 000 molecules was constructed, where the water had a larger area of contact than the original model (Figure 6(a-ii)).
4. The equilibrium state is shown in Figure 6(b-ii), which indicates that the larger initial contact area leads to a larger equilibrium contact area.
5. Results from both an initial wetted contact and a larger area contact indicate that the equilibrium states were highly dependent on the initial state of the water model.

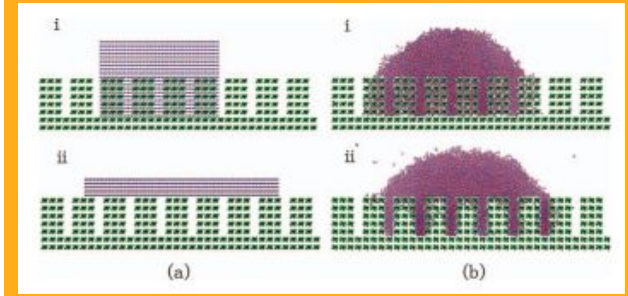

Fig. 6. Snapshots of initial states for (a-i) wetted contact and (a-ii) larger area contact. Equilibrium states for (b-i) wetted contact and (b-ii) larger area contact

Some Additional Results

Through careful observation of the behavior of water molecules on the different pillar surfaces, different spatial distribution regularities were found. Random distributions of water molecules were observed on the P1 and P2 surfaces. The water molecules in the random distribution were similar to the molecules above the surface, and the pinning effect of the pillars on the droplet was remarkable. However, layered distributions were found on the P3 and P4 surfaces.

1. The layered water molecules in this paper were structured and acted as a substrate
2. The pinning effect of the pillars was weak, which resulted in that the pillar surfaces behaving as flat surfaces. This is the reason why the contact angles remained stable when the droplet size was varied.
3. Due to the chain structure of the PTFE model, some differences existed in the pillar dimensions between the horizontal and perpendicular directions.
4. Along with the difference in the distribution of water molecules, the orientations of OH bonds were different between the two equilibrium states

4. Conclusion

This paper provided a molecular-level description of the wetting behaviour of nanosized droplets on the solid surface of PTFE.

Some of the key conclusions drawn are :-

1. The effect of the cutoff of the interatomic potential on the simulation accuracy.
2. On flat surfaces, contact angles of the PTFE surface were near 90° and independent of droplet size.
3. On pillar surfaces, wetted contact and cross-contact appeared.
   a. For wetted contact, contact were dependent on droplet size and pillar dimensions within a certain range.
   b. For cross contact, contact angle values remained stable.
4. Additional simulations indicate final state depends on the initial geometry and and cross-contact is a metastable wetting state.

References

- Molecular dynamics simulations of wetting behavior of water droplets on polytetrafluorethylene surfaces.
  Chen S, Wang J, Ma T, Chen D. J Chem Phys. 2014 Mar 21;140(11):114704. doi: 10.1063/1.4868641. PMID: 24655195.
  (PDF) Molecular dynamics simulations of wetting behavior of water droplets on polytetrafluorethylene surfaces (researchgate.net)
- Evaporation of water in hydrophobic confinement
  S. Sharma and P. G. Debenedetti, Proc. Natl. Acad. Sci. U.S.A. 109, 4365 (2012).
  https://www.pnas.org/content/109/12/4365
- Enhanced Hydrophobicity of Rough Polymer Surfaces
  J. T. Hirvi and T. A. Pakkanen, J. Phys. Chem. B 111, 3336 (2007)
  https://pubs.acs.org/doi/10.1021/jp067399j

Thank You